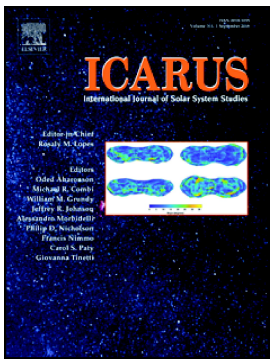

Time variability of the Enceladus plumes: Orbital periods, decadal periods, and aperiodic change

Andrew P. Ingersoll, Shawn P. Ewald, Samantha K. Trumbo

PII: S0019-1035(19)30118-6
DOI: https://doi.org/10.1016/j.icarus.2019.06.006
Reference: YICAR 13345

To appear in: *Icarus*

Received date: 15 February 2019
Revised date: 24 May 2019
Accepted date: 10 June 2019

Please cite this article as: A.P. Ingersoll, S.P. Ewald and S.K. Trumbo, Time variability of the Enceladus plumes: Orbital periods, decadal periods, and aperiodic change, Icarus, https://doi.org/10.1016/j.icarus.2019.06.006

Time Variability of the Enceladus Plumes: Orbital Periods, Decadal Periods, and Aperiodic Change

Andrew P. Ingersoll[a], Shawn P. Ewald[a], Samantha K. Trumbo[a]

[a]Planetary Science 150-21

California Institute of Technology

Pasadena, CA 91125, USA

api@gps.caltech.edu, spe@caltech.edu, strumbo@caltech.edu

February 14, 2019; May 23, 2019

Corresponding author: Andrew P. Ingersoll 626-395-6167

Keywords: Enceladus; Saturn satellites; Tides, solid BODY

Abstract

The Enceladus plumes vary on a number of timescales. Tidal stresses as Enceladus revolves in its eccentric orbit lead to a periodic diurnal variation in the mass and velocity of solid particles in the plume. Tidal stresses associated with an orbital resonance with Dione lead to a periodic decadal variation. Aperiodic variations occur on time scales of months, and may be due to ice buildup and flow of the walls of the fissures that connect the ocean to the surface. We document these variations using all the relevant data taken by the ISS instrument from 2005 to 2017. Key questions now include how a 5% peak-to-peak variation in orbital eccentricity, which itself is only 0.0045, could lead to a 2-fold decadal variation in plume properties. Another question is how the plumes stay open if ice builds up every month and clogs the vents. Other questions include why the solid particles exit the vents several times slower than the gas, and why the speeds vary inversely with the mass of the plumes. The Cassini data are in, but the modeling has just begun.

1. Introduction

The Enceladus plumes sample the global ocean, and their time variability tells us about the physical connection between the ocean and the surface. This paper expands upon previous papers, and uses data from the Imaging Science Subsystem (ISS) of the Cassini spacecraft. We study the plumes' brightness, which is related to the mass flux of solid particles, and the vertical distribution of brightness, which is related to the velocity of the particles. We study the degree of collimation of individual jets. We compare the particulate component of the plumes to the gaseous component, and we discuss how they are coupled. The data span the period from 2005 to 2017, and we use all the observations for which there is an adequate background without shadows, electronic noise, or excessive cosmic rays on the detector. This large data set allows us to separate periodic variations at tidal frequencies from aperiodic variations intrinsic to the vents. The periodic variations arise from Enceladus' revolution around Saturn, which has a period of 1.37 days, and from Enceladus' resonance with Dione, which has periods of 3.9 and 11.1 years. The aperiodic variations may have a variety of sources, but we can identify a timescale that hints at a source mechanism.

Hedman et al. (2013) showed that the brightness of the plume and the launch velocity vary periodically with position in the satellite's eccentric orbit. They showed that the 2005 observations yield brightness levels that are roughly 50% higher than later observations. Hedman et al. used data from the Visible and Infrared Mapping Spectrometer (VIMS) to measure brightness. Nimmo et al. (2014) followed with data from the ISS, and showed that the plumes are brightest near apocenter. Ingersoll and Ewald (2017) hereinafter IE17 also used ISS data and found a 4-fold variation in brightness around the orbit with a maximum at apocenter. All of these results were expressed as integrals over horizontal slabs extending out to infinity. Each group had its own method of background

subtraction, which is a critical part of the analysis because Enceladus and its plumes are imbedded in Saturn's E ring. IE17 confirmed the slower launch speed for the particles at apocenter and the factor of 2 decrease in overall brightness from 2007 to 2015. They noted that the eccentricity of the orbit had decreased by 5% of its value as part of the decreasing phase of a known ~11-year tidal cycle, and offered this as a possible cause of the decadal brightness decrease. Porco et al. (2018) used ISS data from 2006-2017, which they found were best fit by a pair of sinusoids with periods of ~4 years and ~11 years, in agreement with known tidal periods. Here we examine the phase and functional form rather than simply the periods of the decadal signal, to test the hypothesis of long-term tidal forcing.

There are five observational sections in the paper and a final discussion section. Section 2 presents new information about the orbital phase curve. Section 3 presents new evidence that plume activity is strongly affected by a decadal tide. A key step is to remove the diurnal signal so as to examine the decadal signal by itself. Section 4 compares the gaseous and solid components of the plumes and gives evidence that they vary together so as to maintain a constant gas to solid ratio. Section 5 gives examples of individual plumes turning on and off from one month to the next. We have only a handful of examples because documenting this kind of aperiodic variability requires pairs of images with nearly identical viewing geometry. Section 6 confirms that particle speeds are slowest near apocenter, when the plumes are brightest. Section 7 is a discussion of results and unanswered questions. We feel that existing data, used to constrain models currently under development, will lead to a much greater understanding of the ocean-surface interaction. For a general review, see Spencer et al. (2018).

2. Orbital phase curve

Figure 1 shows slab density vs. mean anomaly from 2005-2017. Slab density at 100 km is the inferred particle mass per unit thickness (kg km^{-1}) in a horizontal slab 100 km above the south pole extending to infinity in all horizontal directions. Mean anomaly (MA) is time from pericenter multiplied by 360° and divided by the orbit period. IE17 used data from 2005-2015, but the data from 2005 were sparse and the 2015 data ended in the middle of the year. The mission ended on September 15, 2017, and data from the last two years of the mission are important because they complete the 11-year component of the decadal tide. The data processing, including background subtraction and particle size distribution, was the same as that used in producing Figure 8 of IE17. The particle size distribution is an analytic function whose mass distribution falls off as r^{1} at small radii and r^{-3} at large radii with a median radius of 3.6 μm. The only changes from IE17 are the colors assigned to years 2005-2007 (data from 2017 are colored black) and two years of additional data from the middle of 2015 to the middle of 2017.

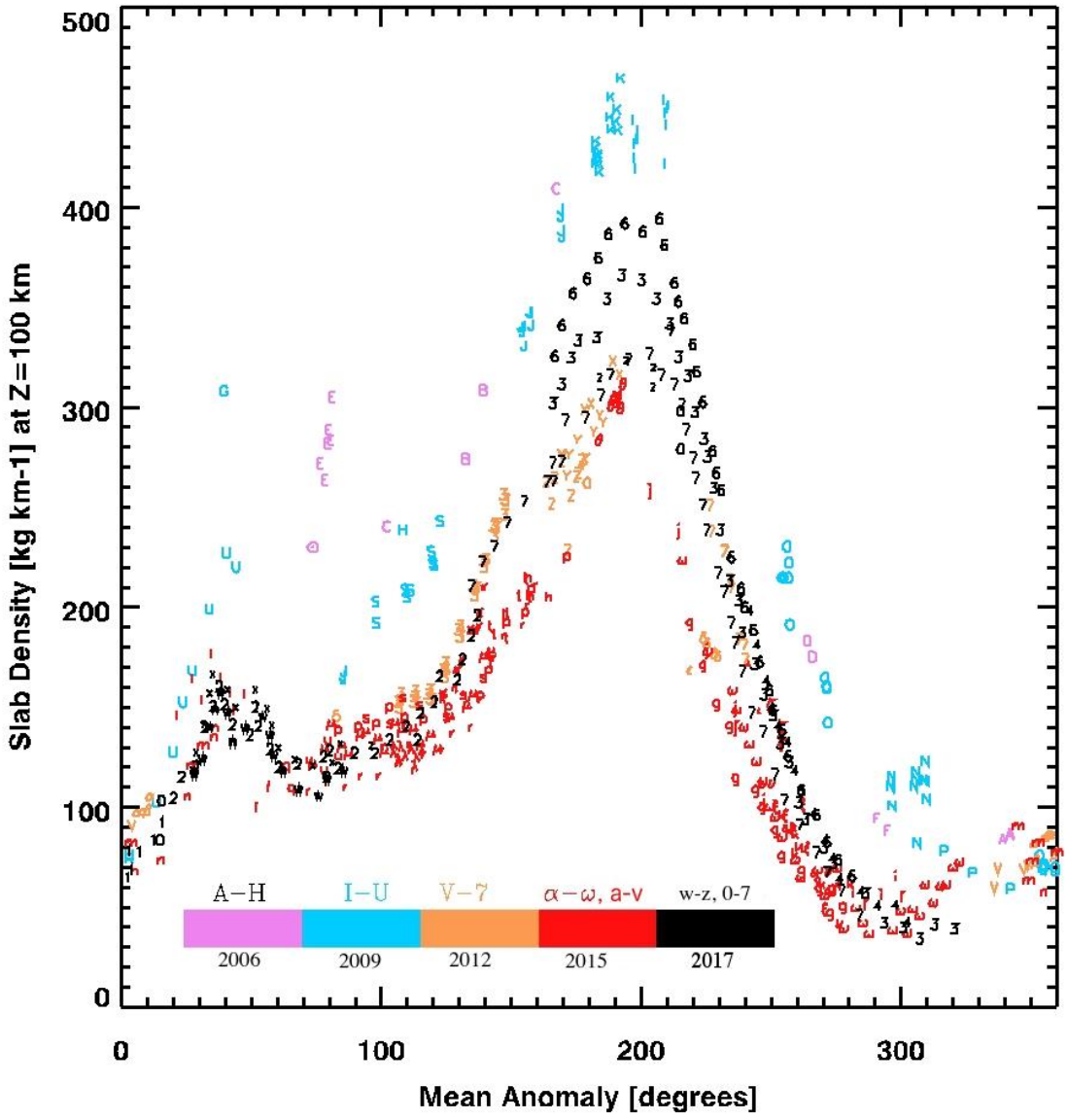

FIGURE 1. SLAB DENSITY VS. MEAN ANOMALY (MA) GROUPED INTO 3-YEAR INTERVALS (2005-2007,..., 2014-2016, 2017). ALL OBSERVATIONS ON THE SAME DAY HAVE THE SAME ALPHANUMERIC SYMBOL. OBSERVATIONS IN THE SAME 3-YEAR GROUP HAVE THE SAME COLOR. EACH DAY, WITH ITS SYMBOL, START/STOP VALUES OF MA, START/STOP VALUES OF SPACECRAFT LONGITUDE, AND A THINNING FACTOR FOR DAYS WITH MANY OBSERVATIONS, IS LISTED IN TABLE 1. EACH OBSERVATION ON EACH DAY IS GIVEN IN TABLE S2 OF THE SUPPLEMENTARY MATERIAL. SOME POINTS THAT WERE USED IN IE17 WERE LATER REJECTED, SO THERE ARE OCCASIONAL GAPS IN THE ALPHANUMERIC

sequence. Reasons for rejection are given in Table S3 of the Supplementary Material. Also, the numbers 0, 3, 5, and 7 were used twice, once for days in 2011-2012 (orange) and again for days in 2017 (black).

The conversion from brightness to column density (mass/area) at a given scattering angle and wavelength depends on the particle size distribution and density. Ingersoll and Ewald (2011) hereinafter IE11 solved for the particle size distribution using observations at very low scattering angles (2-6°) assuming the particles were spheres of solid water ice. In Figure 1 the circle with a dot at the center at MA = 50° is from IE11 and was taken during solar eclipse at a scattering angle of 2.38°. The fact that it agrees with the E observations, taken only 7 months later at scattering angles > 15°, is a good test of the particle size distribution. Guo et al. (2016) showed that low-density aggregates could fit the eclipse observations nearly as well as solid spheres and could have up to 7 times less particle mass in the plumes.

Each point in Figure 1 represents a unique image. It is constructed from a single row of pixels perpendicular to the projected spin axis 100 km above the south pole. The ± 10 kg km^{-1} scatter of points around the smooth curves that come from different images on the same day is a good estimate of measurement precision. This is because the processing of each image is independent of that for all the other images. Other types of scatter, e.g., from different days and different years, come from intrinsic temporal variability. Since the uncertainty in kg km^{-1} is roughly independent of the signal amplitude, the signal to noise ratio (SNR) is decidedly better when the signal is larger. The largest slab density is at MA = 200° (just after apocenter), and the smallest is at MA = 320° (just before pericenter), with a factor of 10 between them.

Several things stand out in Figure 1. First, except for a multiplicative factor that depends on the year, the curves have approximately the same shape. Second, the multiplicative factor varies from year to year. For example, the purple points (2005-2008) and the light blue points (2008-2010) are the highest, and the red points (2014-2016) are the lowest, with the light blue points about twice as high as the red points. These relations are more obvious near MA = 200° where the SNR is large, and are less obvious at MA = 300°-360° where the SNR is small. Third, after a decade of falling brightness in 2006-2014, there is a recovery toward the end, since the black points (2017) are higher than the red points (2014-2016) over most of the range, i.e., from 100° < MA < 300°. Fourth, there is a secondary maximum in slab density with two peaks, one at MA = 36° and the other at MA = 51°.

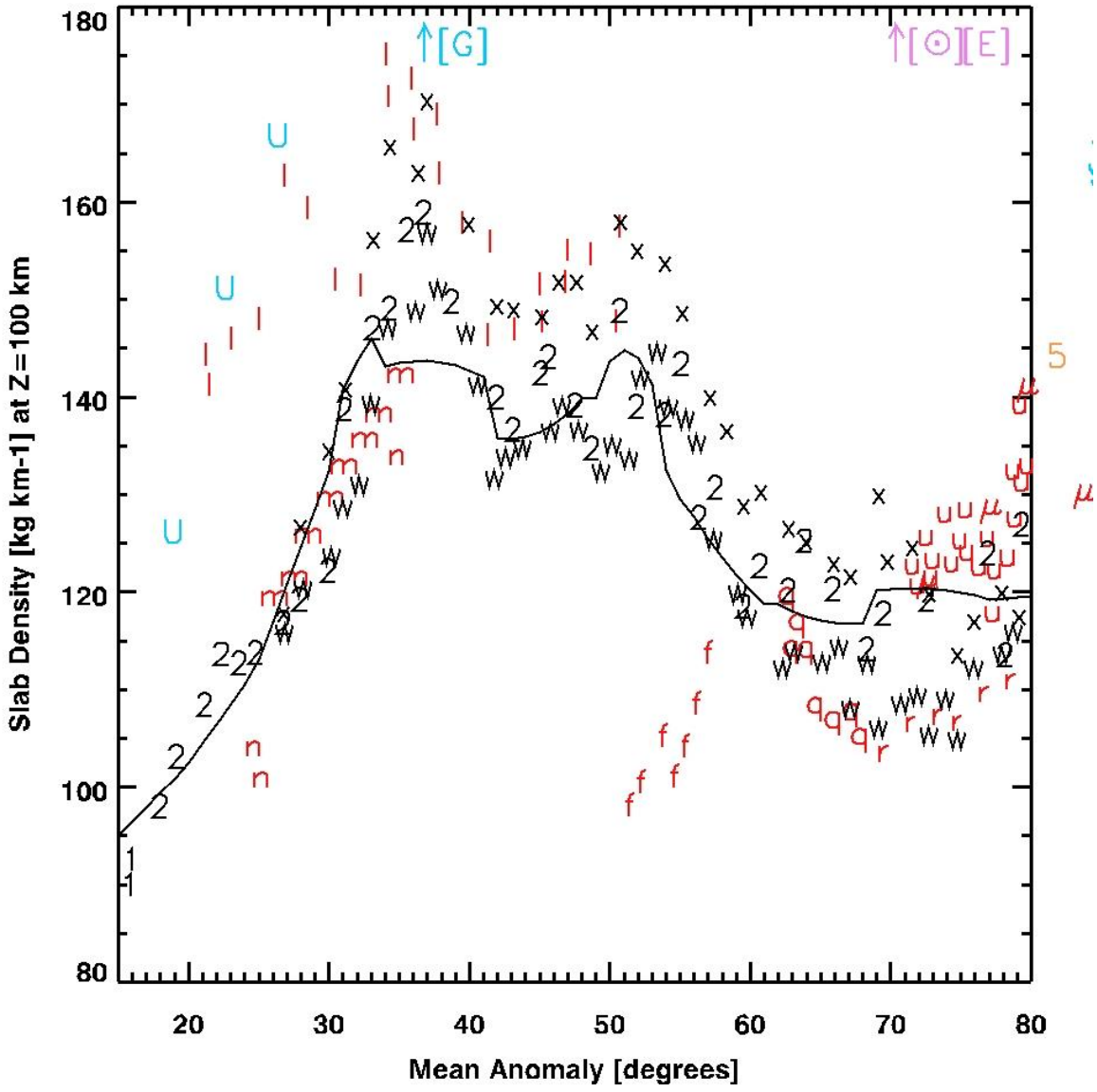

FIGURE 2. SLAB DENSITY AT 100 KM SHOWING THE SECONDARY MAXIMUM WITH PEAKS AT MA 36° AND 51°. THIS IS THE SAME DATA WITH THE SAME COLOR CODING AND ALPHANUMERIC IDENTIFIERS AS IN FIGURE 1. THE POINTS ON THIS FIGURE ARE *L, M, W, X, 2,* AND *D F*. WITH THE EXCEPTION OF *E*, ⊙, and *G*, WHICH ARE OFF SCALE AT THE TOP (INDICATED BY ARROWS), AND THE *F*'S, THE POINTS ARE TIGHTLY BUNCHED AND TRACE OUT A SINGLE CURVE OF SLAB DENSITY VS. MA. POINTS *E*, ⊙, and *G* ARE HIGH BECAUSE THEY WERE TAKEN NEAR THE PEAK OF THE 11-YEAR TIDAL CYCLE, AND THE *F* POINTS ARE LOW BECAUSE THEY WERE TAKEN NEAR A LOW POINT IN THE 11-YEAR TIDAL

cycle. These points do not stand out as much in later figures, where they are grouped with points at the same phase of the tidal cycle.

Figure 2 shows the secondary maximum in greater detail than in Figure 1. The secondary maximum spans the range from MA = 25° to MA = 60°, which is ahead of the primary maximum at mean anomaly ≈ 200°. It is present in the data of Hedman et al. (2013), but Helfenstein and Porco (2015) were the first to point it out in a publication.. Figure 2 shows that the secondary maximum really has two peaks, one at MA = 36° and the other at MA = 51°. The secondary maximum does not appear in the model of Hurford et al. (2007), which has tiger stripes opening and closing in phase with the orbital cycle. Helfenstein and Porco (2015) suggest that the secondary maximum may be due to cross-cutting fractures that open and close at different times than the tiger stripes. They further suggest that additional modeling work is needed to fully understand the simultaneous tidal dilation of tiger stripes and cross-cutting fractures. We do not disagree with Helfenstein and Porco, but we feel that other processes, discussed in section 7, might also contribute to the secondary maximum.

Table 1. Listing of days on which observations were taken. Most days have more than one observation. The symbols are those used in the figures. East longitude may be positive or negative. On some days it was necessary to apply a thinning factor N, which indicates that only 1/N of the observations are shown in the figures. A thinning factor of 1 indicates that all the observations are shown.

Day	Symbol	MA start	MA stop	E Lon start	E Lon stop	Thin
2005 FEB 17	A	338	341	120	118	1
2005 NOV 27	B	130	137	116	100	1
2006 JAN 18	C	100	166	-96	-167	1
2006 MAY 03	D	262	264	47	45	1

2006 SEP 15	⊙	71	71	77	69	1
2007 APR 24	E	75	80	128	122	1
2007 SEP 30	F	289	293	71	67	1
2008 DEC 26	G	38	38	-161	-161	1
2009 MAR 21	H	107	107	-31	-31	1
2009 OCT 13	I	196	210	-134	-134	1
2009 NOV 01	J	84	168	64	56	1
2009 NOV 02	K	181	190	-163	88	1
2009 DEC 25	N	294	308	-20	-23	1
2010 JAN 26	O	254	270	-26	-36	1
2010 MAR 01	P	315	341	-98	-123	1
2010 MAR 02	Q	351	357	-135	-142	1
2010 APR 26	@	252	252	-45	-45	1
2010 MAY 17	R	1	1	-125	-125	1
2010 OCT 16	S	96	121	49	34	1
2010 DEC 20	U	357	42	154	50	1
2011 JAN 30	V	334	2	141	106	1
2011 OCT 01	X	177	190	-144	-156	1
2011 OCT 19	Y	168	184	-141	-155	1
2011 NOV 05	Z	162	177	-141	-154	1
2011 NOV 06	0	178	178	-151	-151	1
2012 MAR 27	3	105	146	-155	-155	1
2012 MAY 01	5	81	81	-121	-154	1
2012 SEP 03	7	225	239	-111	-111	1
2012 SEP 24	α	350	9	78	70	1
2012 OCT 17	β	350	9	-28	-37	1
2012 DEC 09	δ	223	228	-31	-43	1
2012 DEC 23	ε	218	218	47	44	1
2013 JAN 18	ζ	248	253	65	65	1
2013 FEB 25	ϑ	182	192	20	18	1
2013 APR 02	ι	240	245	8	5	1
2013 JUN 12	ϰ	122	138	89	75	1
2013 JUN 24	ƛ	103	114	116	104	1
2015 MAY 10	μ	72	140	-71	-130	1
2015 MAY 31	ν	245	275	142	110	1
2015 JUL 08	ξ	251	275	129	103	1
2015 JUL 29	ω	214	321	145	40	1
2015 OCT 14	f	51	57	-64	-67	32
2015 OCT 15	g	217	279	113	59	6
2015 OCT 28	h	155	165	141	133	11

2015 OCT 29	i	281	303	47	32	12
2015 DEC 07	j	203	247	122	78	3
2015 DEC 08	k	257	280	69	51	3
2016 JAN 02	l	21	50	-43	-66	3
2016 JAN 14	m	343	34	-44	-66	7
2016 SEP 25	n	353	34	-107	-155	1
2016 DEC 06	p	82	176	134	40	2
2017 JAN 25	q	62	67	140	134	5
2017 JAN 26	r	69	158	132	42	6
2017 FEB 08	s	93	140	94	50	6
2017 FEB 09	t	141	157	49	35	3
2017 MAR 09	u	71	82	108	96	9
2017 MAR 31	w	26	84	154	90	11
2017 APR 27	x	26	87	138	72	7
2017 APR 28	y	88	88	71	71	1
2017 MAY 29	z	79	203	57	-38	2
2017 MAY 30	0	214	14	-46	138	1
2017 JUN 11	1	1	15	141	125	6
2017 JUN 12	2	17	135	122	12	7
2017 JUN 18	3	164	320	-15	-169	7
2017 JUL 14	4	240	306	-92	-167	7
2017 AUG 02	6	165	282	-33	-150	5
2017 AUG 28	7	133	283	-18	-166	5

3. Decadal tide

Figure 3 shows the template that we use to remove the MA signal in order to study the longer timescale variations. Based on Figure 1, we assume that the distribution of points from one day to the next remains the same except for a multiplicative constant. This is an empirical parameterization of the diurnal cycle; it has no theoretical basis. Dividing by the template gives the value of the constant, which ideally varies with the decadal cycle but not with the diurnal cycle. In creating the template, we mainly used points from days 2 and 7, which are from 2017. Taking the average over all years has problems because the early observations are sparse and cover only a small range of MA. In contrast,

WITH A SMALL AMOUNT OF INTERPOLATION, DAYS 2 AND 7 COVER AN ENTIRE ORBITAL CYCLE. THE UNITS OF THE TEMPLATE ARE THE SAME AS THOSE IN FIGURE 1.

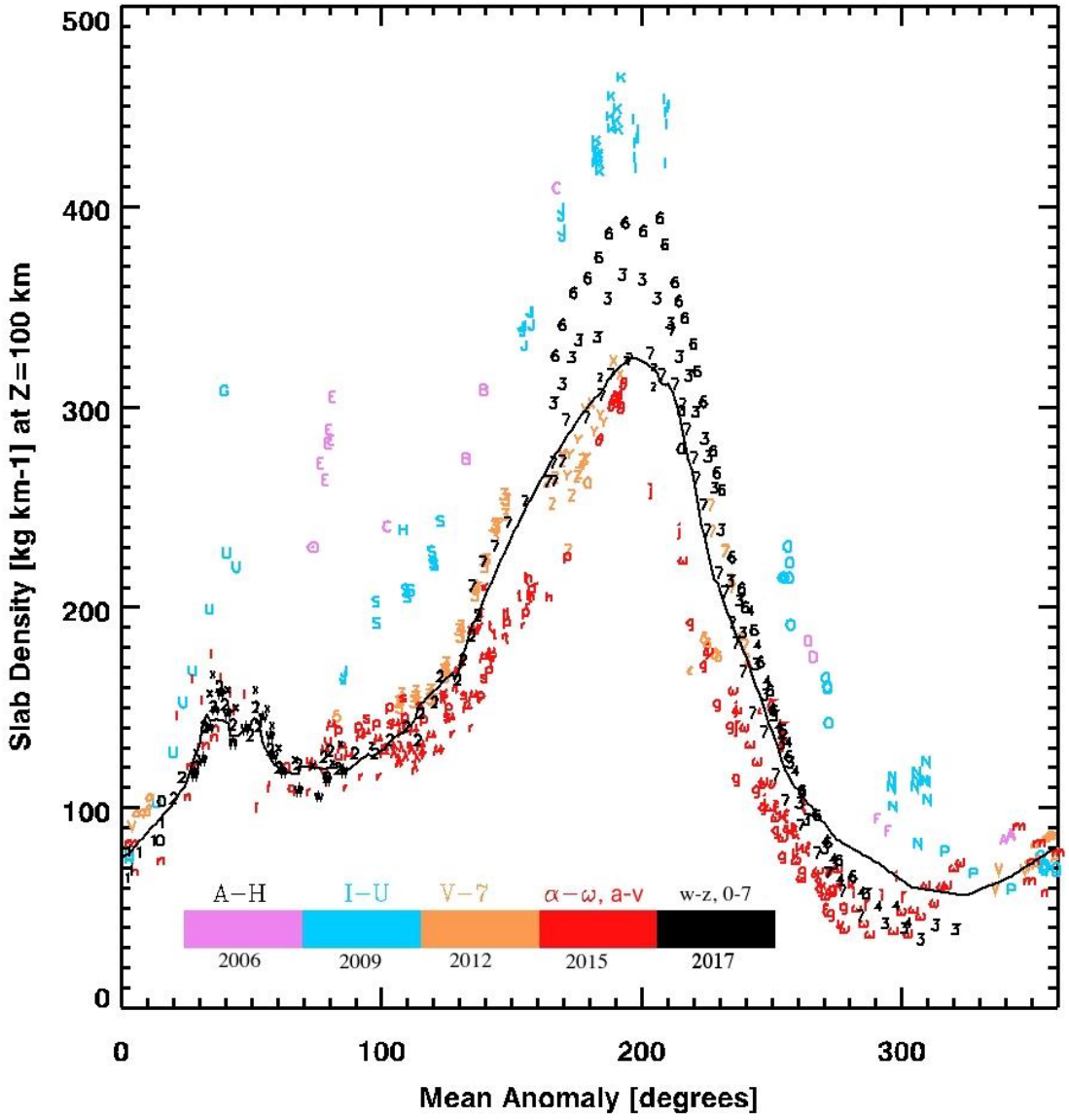

FIGURE 3. SLAB DENSITY VS. MEAN ANOMALY WITH THE TEMPLATE SUPERPOSED ON THE DATA OF FIGURE 1. THE TEMPLATE IS CONSTRUCTED MOSTLY FROM DATA ON DAYS 2 AND 7, WHICH ARE FROM JUNE 12, 2017 AND AUGUST 28, 2017 RESPECTIVELY. INTERPOLATION WAS USED BETWEEN MA = 260° AND MA = 360°, AND WAS CHOSEN AS A COMPROMISE BETWEEN DAYS N AND DAYS ω, WHICH ARE FROM DECEMBER 25, 2009 AND JULY 29, 2015, RESPECTIVELY (TABLE 1).

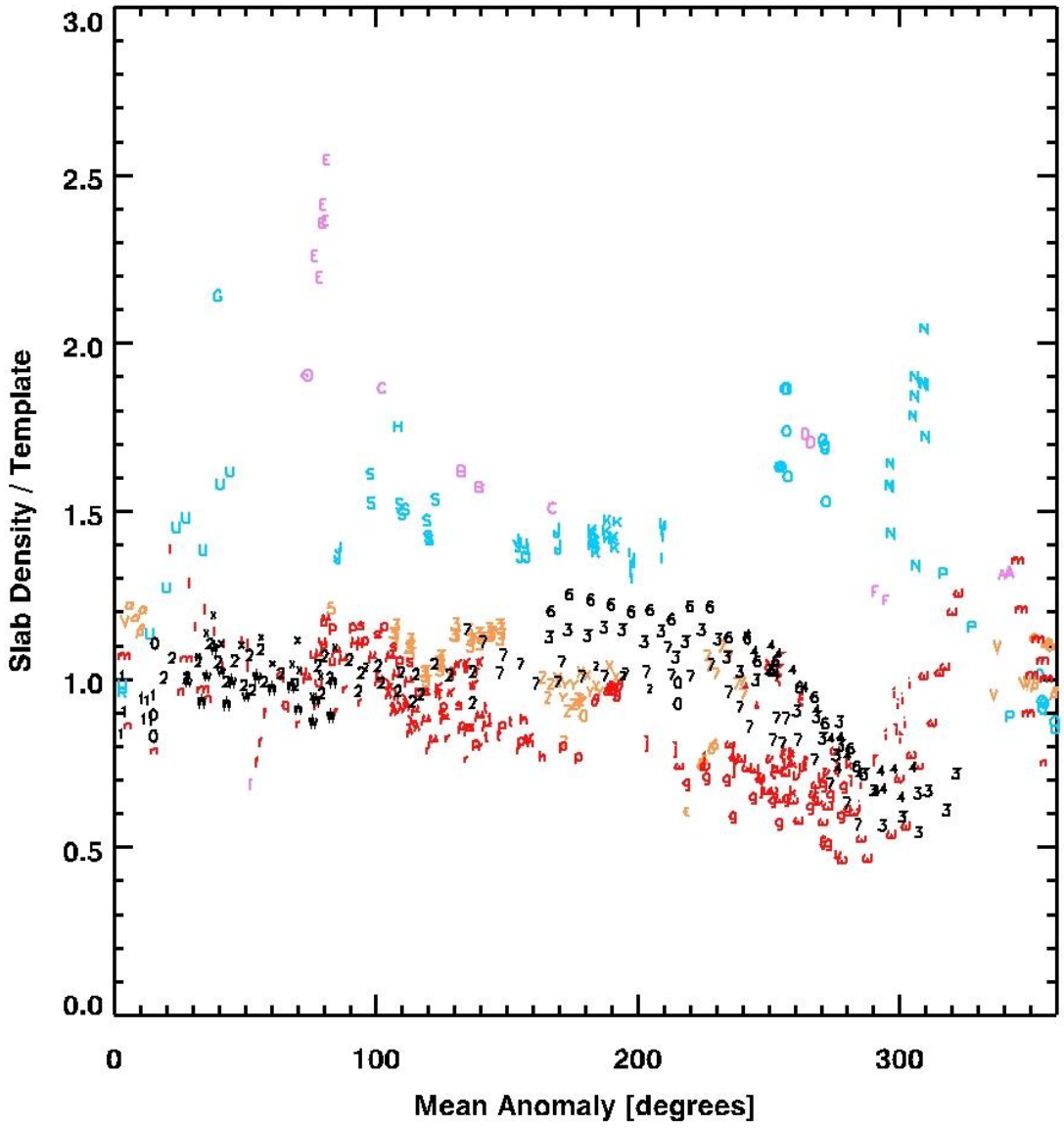

FIGURE 4. RATIO OF SLAB DENSITY OF THE POINTS IN FIGURE 1 TO THE SLAB DENSITY OF THE TEMPLATE, PLOTTED AGAINST MA. THE ALPHANUMERIC SYMBOLS AND THE COLORS ARE THE SAME AS THOSE IN FIGURE 1. SINCE THE TEMPLATE IS DERIVED MOSTLY FROM DAYS 2 AND 7, THOSE DAYS APPEAR NEAR UNITY ACROSS THE GRAPH.

FIGURE 4 SHOWS THE SLAB DENSITY OF EACH POINT IN FIGURE 1 DIVIDED BY THE SLAB DENSITY OF THE TEMPLATE, PLOTTED AGAINST MA. IF THE SHAPE OF THE

diurnal curve were exactly constant and if the multiplicative constant were changing on decadal timescales, the points would form a stack of horizontal layers varying continuously with time. The 3-year color bands would turn the stack into layers of finite thickness. The horizontal layering is most pronounced in the range MA = 120-240°. There the SNR is highest because measured slab density (the signal) is large and the uncertainty of the measurement (the noise) is roughly independent of slab density. One sees that (slab density)/template for the light blue points and the red points are about 1.5 and 0.75 respectively, confirming the factor of 2 ratio of light blue to red shown in Figure 1. As shown in Figure 1, slab density is smallest around MA = 320°, and there the spread of the points in Figure 4 is greatest. If we had chosen higher values for the interpolated portion of the template (MA = 260° to MA = 360°), the ω points would be much less than one, and if we had chosen the interpolated portion much lower, the N points would shoot off to unrealistically high values. The fitting was done by eye. A weighted average would seem more rigorous, but choosing the weights and which points to focus on would make it equally subjective. The points in Figure 4 are ratios, and ratios are particularly sensitive to noise because the denominator can approach zero when the uncertainty is large.

Figure 5 tests the hypothesis that there is a linear relationship between (slab density)/template and orbital eccentricity. The x-axis is Δr, the Saturn-Enceladus distance at apocenter minus that at pericenter. For a Keplerian ellipse, $\Delta r = 2AE$, where A is the semi-major axis and E is the eccentricity, respectively. The y-axis gives the alphanumeric characters, which are obtained from Figure 4 by averaging all the (slab density)/template measurements in each day into a single number for that day. The straight line is y = m*x + b, and it is a least-squares fit to the data, with m = 0.006527 km^{-1} and b = -13.62.

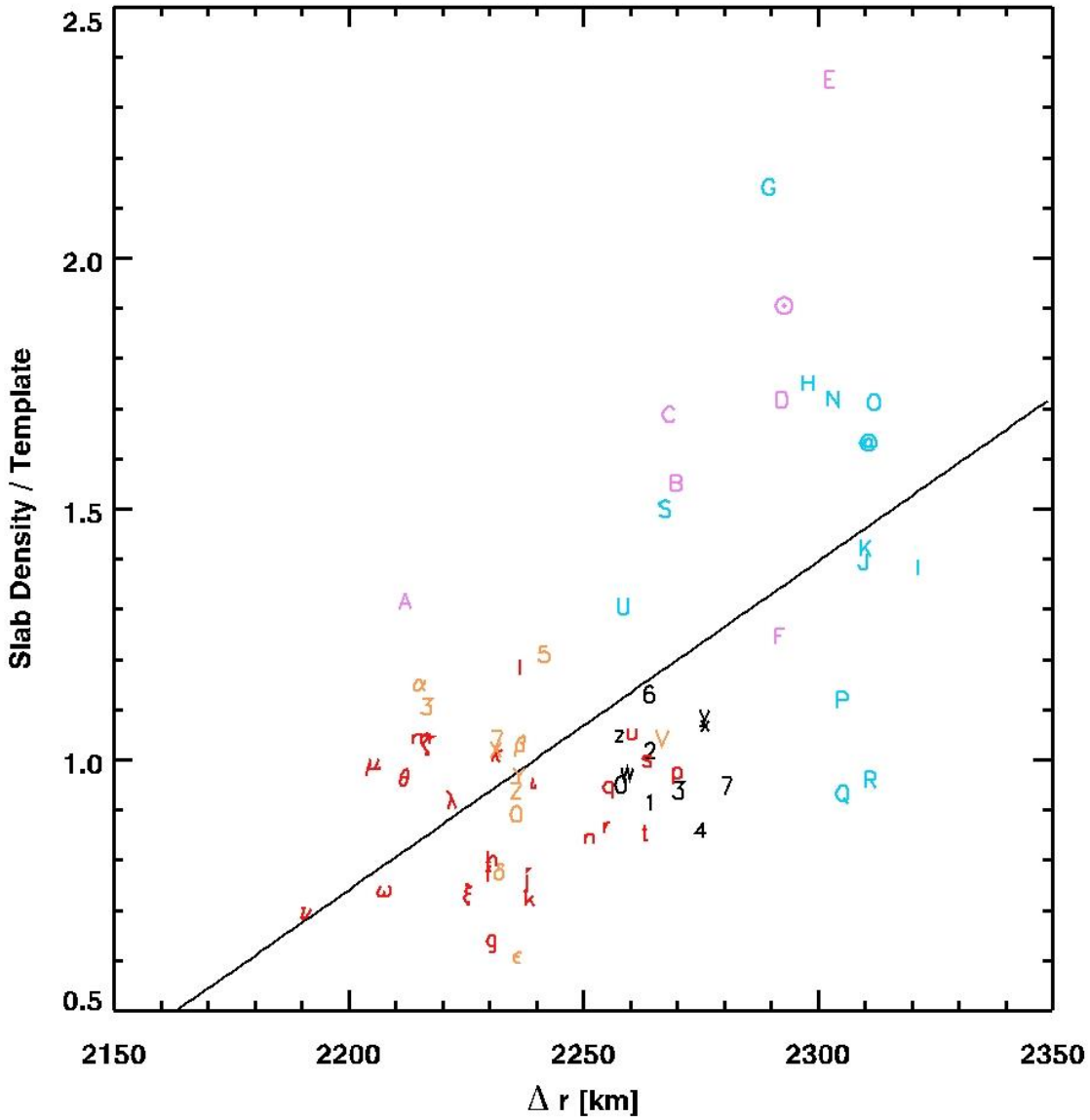

FIGURE 5. LEAST SQUARES FIT TO THE DATA OF FIGURE 3 AND 4. EACH POINT IS ONE DAY'S WORTH OF OBSERVATIONS PROCESSED TO REMOVE THE DEPENDENCE ON MA AND REVEAL THE DECADAL TIMESCALE VARIABILITY. THE COLORS AND SYMBOLS ARE THE SAME AS IN FIGURE 1. THE Y AXIS IN THE MEASURED SLAB DENSITY FROM FIGURE 1 DIVIDED BY THE TEMPLATE IN FIGURE 3. THE X AXIS IS THE APOCENTER MINUS PERICENTER DISTANCE, WHOSE DOMINANT PERIODS OF VARIATION ARE 11.1 YEARS AND 3.9 YEARS ACCORDING TO VIENNE AND DURIEZ (1991).

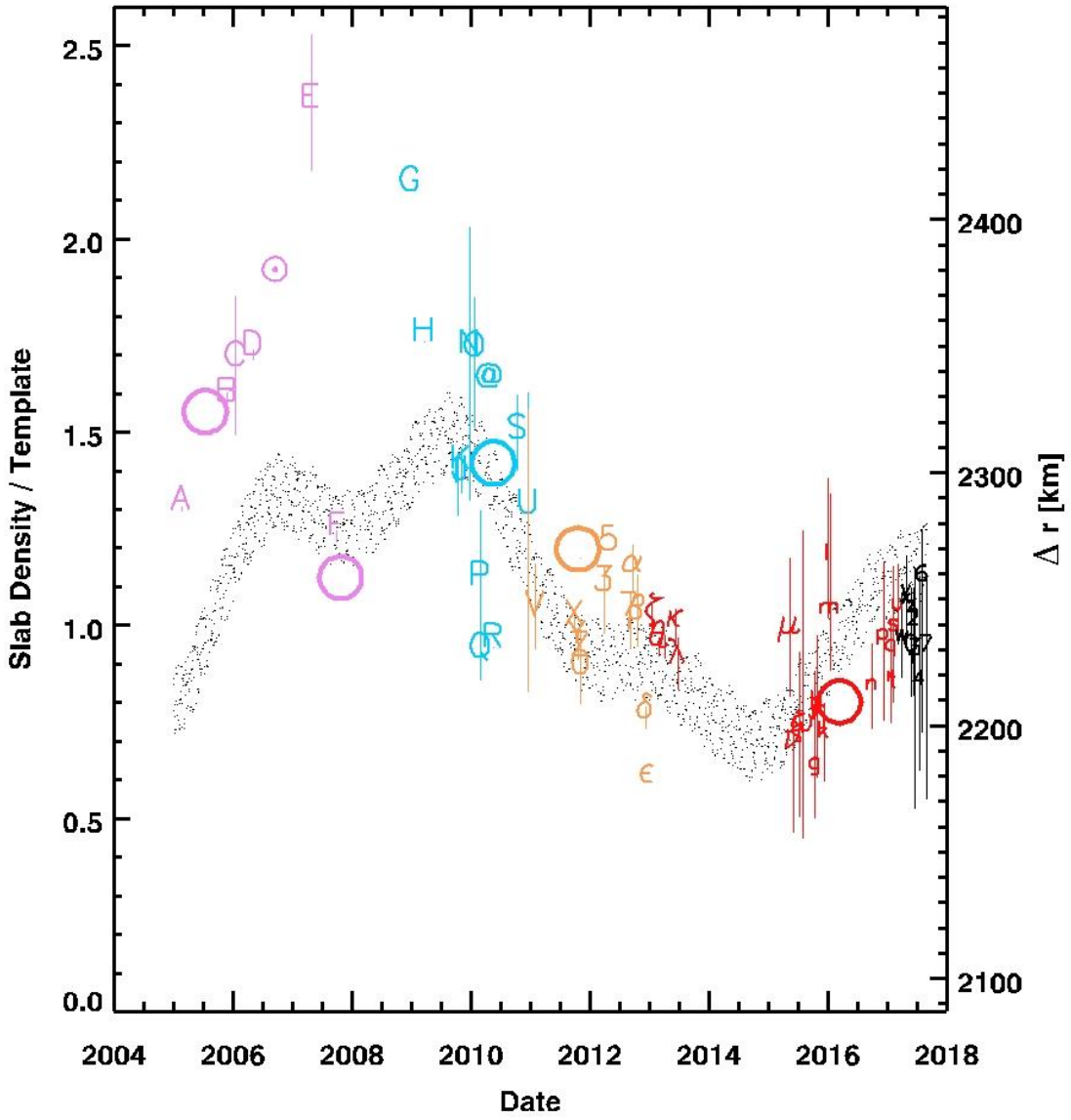

FIGURE 6. AS IN FIGURE 4 BUT THE RATIO (SLAB DENSITY)/TEMPLATE IS PLOTTED AGAINST TIME. THE EVEN YEARS BEGIN ON THE LARGE TICK MARKS; THE ODD YEARS ARE IN BETWEEN. LEFT AXIS: ALPHANUMERIC SYMBOLS AND THE COLORS ARE THE SAME AS THOSE IN FIGURES 4 AND 5. VERTICAL LINES SHOW THE EXTREMES FOR DAYS WHERE INDIVIDUAL IMAGES ON THAT DAY HAVE BEEN AVERAGED TOGETHER. RIGHT AXIS: DIFFERENCE ΔR BETWEEN THE MAXIMUM AND MINIMUM DISTANCE FROM ENCELADUS TO SATURN CALCULATED USING NAIF/SPICE. EACH POINT IN THE CLOUD OF POINTS IS A SINGLE ORBIT, AND THERE ARE THOUSANDS OF ORBITS. THE SPREAD OF

THE POINTS IS DUE TO DAILY INTERACTIONS WITH THE OTHER SATELLITES. THE MULTI-YEAR VARIATIONS ARE DUE TO A RESONANCE BETWEEN ENCELADUS AND DIONE AND HAVE DOMINANT PERIODS OF 11.1 YEARS AND 3.9 YEARS. THE RIGHT AXIS AND THE CLOUD OF POINTS HAVE BEEN SCALED TO HAVE THE SAME AMPLITUDE VARIATIONS AS THE LEFT AXIS, AND HAVE BEEN SHIFTED VERTICALLY TO ALIGN THE VARIATIONS HORIZONTALLY ON THE FIGURE. THE VALUES OF THESE ADJUSTMENTS WERE CHOSEN FROM THE LINEAR LEAST SQUARES FIT ILLUSTRATED IN FIGURE 5. THESE ADJUSTMENTS AFFECT RELATIVE AMPLITUDES BUT NOT THE SHAPE OR PHASING OF THE CURVES. THE FIVE CIRCLES ARE THE UVIS OBSERVATIONS WITH THEIR OWN SCALING FACTOR. THEY ARE DISCUSSED IN SECTION 4 IN CONNECTION WITH FIGURE 7.

FIGURE 6 SHOWS THE TWO VARIABLES OF FIGURE 5 PLOTTED AGAINST TIME FROM 2005-2017. THE VERTICAL SCALE ON THE LEFT IS SLAB DENSITY DIVIDED BY TEMPLATE, AND THE ALPHANUMERIC CHARACTERS ARE PLOTTED ON THIS SCALE. THE VERTICAL SCALE ON THE RIGHT IS ΔR, AND THE CLOUDS OF DOTS ARE PLOTTED ON THIS SCALE. THE ZERO OFFSET, WHICH IS THE VALUE OF ΔR WHERE THE SLAB DENSITY Y IS 0, IS AT $\Delta R = -B/M = 2087$ KM. THE SCALE FACTOR, WHICH IS THE ΔR UNIT ON THE RIGHT THAT IS EQUIVALENT TO 1 UNIT ON THE LEFT,
IS $1/M = 153.2$ KM. THE NUMBERS B AND M COME FROM THE LEAST SQUARES FIT IN FIGURE 5.

THE HYPOTHESIS BEING TESTED IS THAT THE ALPHANUMERIC CHARACTERS AND THE CLOUD OF DOTS ARE RELATED. THE SHAPES OF THE TWO CURVES ARE WHAT MATTER, SINCE THEY ARE UNAFFECTED BY THE SCALING FACTOR ADJUSTMENT AND ZERO OFFSET. FIGURE 6 RESEMBLES FIGURE 17 OF IE17, WHO PROPOSED THAT THE DECREASE OF SLAB DENSITY OVER MUCH OF THE PERIOD FROM 2005 TO 2015 WAS RELATED TO THE DECLINING PHASE OF THE 11.1-YEAR CYCLE OF ECCENTRICITY. HOWEVER FIGURE 17 OF IE17 PLOTS THE ALPHANUMERIC POINTS ACCORDING TO THEIR ΔR VALUES INSTEAD OF THEIR SLAB DENSITY VALUES.

THE 12-YEAR INTERVAL IS NOT LONG ENOUGH TO ESTABLISH THAT AN 11.1-YEAR CYCLE IS PRESENT IN THE (SLAB DENSITY)/TEMPLATE VARIABLE OF FIGURE 6.

But celestial mechanics tells us that it is present in the ΔR variable, so we can ask, if the cycle were present in both variables, do their phases match? Figure 6 suggests that they do. Both the (slab density)/template points and the ΔR cloud of points have a peak in 2007-2009 and a trough one half cycle later in 2013-2015. There is also a rapid rise near 2006 and a rise in 2017, a full cycle later. The 3.9-year cycle is harder to see. The F point in 2007.5 is a trough between the higher E and G points, and it coincides with a prominent trough in the ΔR cloud. There are no data in the prominent trough at year 2014, but the trends on either side point down toward the center. There is a small trough in year 2011.5, since images on orbits V, X, Y, Z and 0 (January 30, 2011 to November 6, 2011) are lower than those on orbits 3, 5, 7, α and β (March 27, 2012 to October 17, 2012). That trough coincides with a trough in the ΔR data, which suggests a positive phase relation. Thus although there are gaps in the coverage, the data strongly suggest that the quantities plotted on the left and right axes are related. This figure complements the work of Porco et al. (2018), who examined the plume signal in the frequency domain without regard to the phase of the signal.

There are several ways the (slab density)/template points and the ΔR points could fail to overlap, even if they were related. First, variables other than eccentricity might also be affecting the slab density. The template we used was constructed from 2017 observations, and it does a good job of fitting the data starting with I, J, and K in late 2009 and extending through 2017. In contrast, points A-H, which cover the years 2005-2008, seem anomalously high according to Figures 5 and 6, although they have the same double-peaked shape as the cloud of ΔR points. These "errant" data could be explained if the plumes were intrinsically brighter during 2005-2008 for reasons unrelated to eccentricity. Second, our templatized parameterization of the diurnal cycle may be too simple. For instance, the red curves and the black curves cross at MA = 305° and separate again at MA = 70°, despite being obviously separate from 70-330°.

This crossing is most obvious in Figures 1 and 3. The crossing occurs where the signal is low. But the crossing is not the result of random noise, and it cannot be made to disappear simply by adjusting the template in that interval. The crossing could indicate a change in the shape of the diurnal cycle, being relatively brighter from MA = 305° to 70° in the early (red) years compared with the later (black) years. Third, variability of individual plumes, which we document in section 5, could be contributing to variability of slab brightness, especially when the latter is small, as it is from MA = 305° to 70°. An example is the P, Q, and R points. They stand out sharply in Figure 6 at the start of year 2010, but they straddle MA = 360° and thus their amplitude is small and they are sensitive to individual plume variations.

IE17 were cautious in claiming a relation between the decadal change in plume density and the decadal change in orbital eccentricity. They mentioned seasonal change from summer to winter in the south, but the radiative effect seemed too small. Also, the troughs in the years 2007.5 and 2011.5 indicate a period that is considerably shorter than the 30-year annual cycle. IE17 mentioned stochastic variability, but the probability of all the plumes declining together seemed improbable. The decadal change hypothesis has its own problems. The mean eccentricity is only 0.5%, and it is changing by only ±2.5% of itself. Nevertheless, with the 2015-2017 data we are inclined to believe the relation, but we still do not understand it. Perhaps this is a case of self-organized criticality, where the conduits from the ocean to the surface have adjusted themselves so they barely stay open for a given eccentricity. Then the ±2.5% decadal change in eccentricity has a large (factor of 2) effect. As we said in IE17, we need a quantitative theory, but that belongs in another paper.

4. Gas vs. solid particles in the plumes

Plume brightness in Figure 1 is an indicator of *solid* particles in the plume. Hansen et al. (2011) used occultations of stars by the Ultraviolet Spectrometer (UVIS) to measure the amount of water *vapor* in the plume. Using their estimate, IE11 put the ice/vapor mass ratio in the range 0.3-0.70. Gao et al. (2016) noted that if the particles were low-density aggregates, the ice/vapor ratio could be as much as 7 times lower. The Ion and Neutral Mass Spectrometer (INMS) instrument also measures the amount of vapor in the plume. Dong et al. (2015) used INMS data from Teolis et al. (2010). They combined these with nanograin data from the Cassini Plasma Spectrometer (CAPS) and micrograin data from the Radio and Plasma Wave Spectrometer (RPWS) to infer a total grain mass density equal to ~20% of the vapor. Dong et al. (2015) also assumed the particles were solid water ice. Hedman et al. (2018) used a single solar occultation observed simultaneously by VIMS and UVIS to infer the dust-to-gas ratio directly (dust = ice in this context), and found values of ~1 for some tiger stripes and values ~0.1 for others. Hansen et al. (2017) compared five occultations observed by the UVIS and concluded that the bulk water vapor emanating from Enceladus changed very little with orbital position - no more than ±15%. This contrasts with the 4-fold variation of the ice particles reported by IE17 and Nimmo et al. (2014).

Porco et al. (2014) identified 100 jets by triangulation in ISS images taken from a variety of longitudes over a 6.5-year period. They stated that one third of the jets cycled on and off during that period, but they did not constrain the timescale further, e.g., by showing images of individual jets appearing and disappearing. Spitale et al. (2015) argued that much of the jet-like activity could be explained by optical illusions arising when the curtains of dust emanating from the tiger stripes are viewed edge-on. Nevertheless, Teolis et al. (2017) used the locations and directions of the 100 jets identified by Porco et al. (2014) to constrain the half-dozen peaks in three INMS time series from low-altitude flybys. They conclude that the CO_2 gas in individual jets varies by factors up to 10 and the overall vapor

plume source rate exhibits stochastic time variability by up to a factor of ~5 between observations. Yeoh et al. (2017) looked at a different set of INMS data, focused on H_2O vapor, and they found a factor of 2 variability. They find that narrow vapor jets produce better fits to the observations, suggesting high Mach numbers (> 5) at the vents. They find that the distributed sources along the tiger stripes are likely dominant while the jets provide a lesser contribution.

The large variations with orbital position (factors up to 10) seen in INMS data would appear to be inconsistent with the small (±15%) variation seen in UVIS data. However during an orbital pass, UVIS is continuously integrating along the ray path to the star, whereas the INMS is only sampling the immediate environment of the spacecraft. At the end of the orbital pass, UVIS has sampled all the absorbers on a 2D surface above the south pole, whereas INMS has only sampled along a line through the plume. Yeoh et al. (2017) make the same point. With different paths through the plume at different values of MA, it is possible to mistake uneven sampling for stochastic variability.

The 11-year tidal cycle adds a dimension other than MA and stochastic variability to the sample space. But with ~3000 imaging observations on a total of 64 days (Table 1), which are spread over the period from 2005-2017, it is possible to separate the sources of variability. Here we address the apparent disagreement between the 4-fold diurnal variation in slab density seen by ISS (IE17 and this paper) and the ±15% variation in vapor flux seen by UVIS (Hansen et al., 2017).

The disagreement concerns the diurnal variability - variations with respect to MA or lack thereof. Since the observations are spread over 12 years, it is first necessary to remove the decadal variability shown in Figures 5 and 6. Figure 7 shows slab density as in Figure 1 with five circles representing the UVIS observations. To remove the decadal variability,

BOTH DATA SETS WERE "ADJUSTED" BY DIVIDING BY THE FUNCTION Y = M*X + B THAT FITS (SLAB DENSITY)/TEMPLATE AS A FUNCTION OF ΔR (FIGURE 5). DIVIDING BY THIS FUNCTION ASSUMES THAT THE UVIS OBSERVATIONS OF THE VAPOR EXHIBIT THE SAME DECADAL VARIABILITY AS THE ISS OBSERVATIONS OF SLAB DENSITY. THE ADJUSTMENT ALLOWS US TO LOOK AT THE DIURNAL VARIABILITY BY ITSELF, WITHOUT THE MODULATION DUE TO DECADAL VARIABILITY. TABLE 2 GIVES THE DATES OF THE UVIS OCCULTATIONS, THE VALUES OF MA, THE UVIS MASS FLUX, THE VALUE OF ΔR, AND THE SCALED MASS FLUX.

FIGURE 7 SHOWS THAT THE ADJUSTMENT MAKES THE SLAB DENSITY DATA MORE COMPACT, E.G., THE A, B, C, D, ⊙, E AND G POINTS ARE CLOSER TO THE CLUSTER OF POINTS FROM LATER YEARS. FOUR OUT OF FIVE OF THE UVIS POINTS FALL WITHIN THE CLUSTER OF SLAB DENSITY POINTS. THE ONE "ERRANT" UVIS POINT, AT MA = 117°, IS FROM 2005 AND IT FITS IN WITH THE "ERRANT" SLAB DENSITY POINTS C, ⊙, AND E, WHICH ARE ALSO FROM THE EARLY YEARS. NOTICE THAT THERE ARE TWO C POINTS, ONE AT MA = 100° AND THE OTHER AT MA = 166°. THUS ALL FIVE OF THE UVIS POINTS ARE VARYING WITH SLAB DENSITY IN ABOUT THE SAME PROPORTIONS. THE BLACK LINE IS THE TEMPLATE, WHICH IS USED IN FIGURES 4-6 BUT NOT IN THIS FIGURE.

THE UVIS DID NOT SAMPLE THE LARGEST VALUES OF SLAB DENSITY, FROM MA = 117° TO 220°, AND IT DID NOT SAMPLE THE SMALLEST VALUES, FROM 236° TO 98°, BUT FIGURE 7 SUGGESTS THAT THE UVIS MASS FLUX VARIES WITH MA BY THE SAME FACTOR AS SLAB DENSITY. IN OTHER WORDS, THE PARTICLES AND THE VAPOR COULD BE VARYING TOGETHER, MAINTAINING THE SAME SOLID TO VAPOR RATIO THROUGHOUT THE ORBIT ON A DIURNAL TIMESCALE. CO-VARIATION ALSO APPEARS IN FIGURE 6, WHICH IS THE OPPOSITE OF FIGURE 7 BECAUSE IT FOCUSES ON THE DECADAL VARIABILITY. IN FIGURE 6, THE DIURNAL VARIABILITY WAS REMOVED BY DIVIDING BOTH DATA SETS BY THE TEMPLATE INTRODUCED IN FIGURE 3. THE UVIS POINTS WERE MULTIPLIED BY THE SAME 1.0 S/KM SCALE FACTOR AS IN FIGURE 7. FIGURE 6 SHOWS THAT THE FIVE UVIS CIRCLES TRACK THE ΔR CLOUD FAIRLY WELL, INCLUDING THE TROUGH AT YEAR 2007.5 AND THE PEAKS ON EITHER SIDE OF IT. THERE IS EVEN A HINT

of a trough in UVIS that comes close to matching the trough in ΔR at year 2014. The cloud of ΔR points is our best summary of the decadal cycle of slab density, and Figure 6 suggests that it also a good summary of the decadal cycle of UVIS. In other words, both Figure 6 and Figure 7 imply that the vapor and solid particles are varying together.

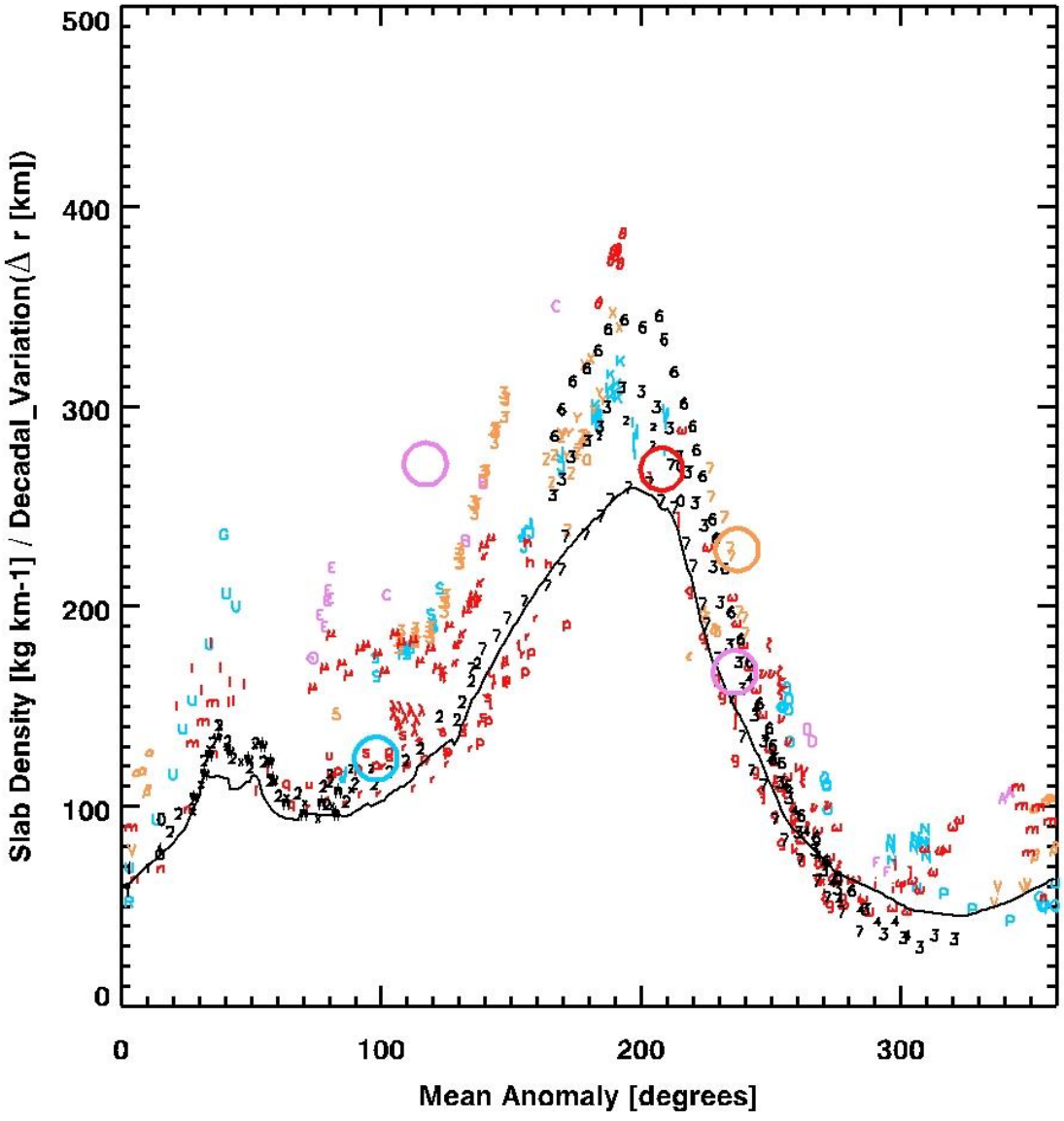

Figure 7. Comparison of slab density in kg/km (alphanumeric symbols) with UVIS vapor flux in kg/s (colored circles). Both data sets are colored according to the 3-year groupings defined in Figure 1. Both data sets have

had the decadal variation removed by dividing by the least squares fit of the (slab density)/template ratio to ΔR. The five UVIS points have been multiplied by a scale factor equal to 1.0 s/km. This multiplication does not change the relative heights and positions of the UVIS points, but it allows them to fit on the same amplitude scale. As discussed in the text, all five of the UVIS points fall among the slab density points from the same years, suggesting that the particles and the vapor are varying together during the diurnal cycle.

Date	MA	UVIS	ΔR	UVIS
	degree	kg/s	km	kg/s, scaled
2005 JUL 14	117	240	2223	269.8
2007 OCT 24	236	210	2280	166.5
2010 MAY 18	98	180	2310	123.5
2011 OCT 19	220	220	2235	227.3
2016 MAR 11	250	250	2230	267.3

Table 2. UVIS stellar occultation results scaled to remove the decadal cycle. The third column gives the vapor mass flux in kg/s reported in Table 2 of Hansen et al. (2017). The fourth column is ΔR, the apocenter minus pericenter distance of the orbit on the date of observation. The fifth column is the fourth column divided by the linear least squares function Y = M*X + B that fits the (slab density)/template data as a function of ΔR (Figure 5). This function best removes the effect of the decadal tide from the slab density data in Figure 1.

4. Aperiodic variability of individual plumes

Ingersoll and Pankine (2010) hereinafter IP10 estimated that condensation on the walls of the cracks could seal them off in a year,

assuming condensation is supplying the 5.8 ± 1.9 GW of radiative heat emanated from the tiger stripes as observed by Spencer et al. (2006) and Abramov and Spencer (2009). The timescale is proportional to crack width, which Nakajima and Ingersoll (2016) hereinafter NI16 give as 0.05-0.075 m in order to match the ~10:1 ratio of radiated heat to latent heat carried with the vapor. Wider cracks would give a lower ratio, because more mass would escape as vapor even though the amount condensing on the walls would not change. Based on their estimate of crack width, NI16 conclude that buildup of ice could seal the cracks off in a few months, but they did not discuss how the overall vent activity is maintained.

In this section we show sequences of images with individual plumes turning on and off. We estimate the characteristic timescale of these changes, and we find one plume that had a 3% effect on the overall slab density. These changes are different from the periodic changes associated with the tides, i.e., the 1.37 day orbital cycle and the decadal timescale changes associated the Dione resonance. The aperiodic changes are a third type of variation, possibly associated with the buildup of ice on the walls of the vents, although we do not understand what keeps the vents open.

In order to search for variability of individual jets within the plume, we examined a large set of 2,405 images, which were treated in Ingersoll and Ewald (2017) and span the years 2005 – 2015. We paid particular attention to the high-resolution images within this set, in which multiple distinct, collimated jets were visible. In order to compare the jets visible in different images and at different viewing geometries, we developed a routine that allowed us to identify the visible jets in a particular image and project line segments where the same jets should be located in other images. We utilized the catalog of ~100 jets from Porco et al. (2014), which includes jet latitudes, longitudes, azimuth angles, and zenith angles, thereby effectively defining each jet in three dimensions within Enceladus' reference frame. In order to calculate the predicted location and orientation of any given jet in a given image, we used the spacecraft

navigation and pointing data for that image, taken from the corresponding SPICE system kernel files. Using this knowledge of the spacecraft's position and orientation relative to Enceladus, we then project the three-dimensional jets into the two-dimensional plane of the image. To perform these calculations, we utilized standard NAIF/SPICE library routines developed for working with spacecraft geometries.

Once we had used this tool to identify cataloged jets in a certain image, we could then project line segments representative of these jets of interest at their expected locations within other images. Each jet was held to a length of 50 km and projected at the pixel scale of the image in question. The above method automatically accounts for the effects of foreshortening on the projected jet segments.

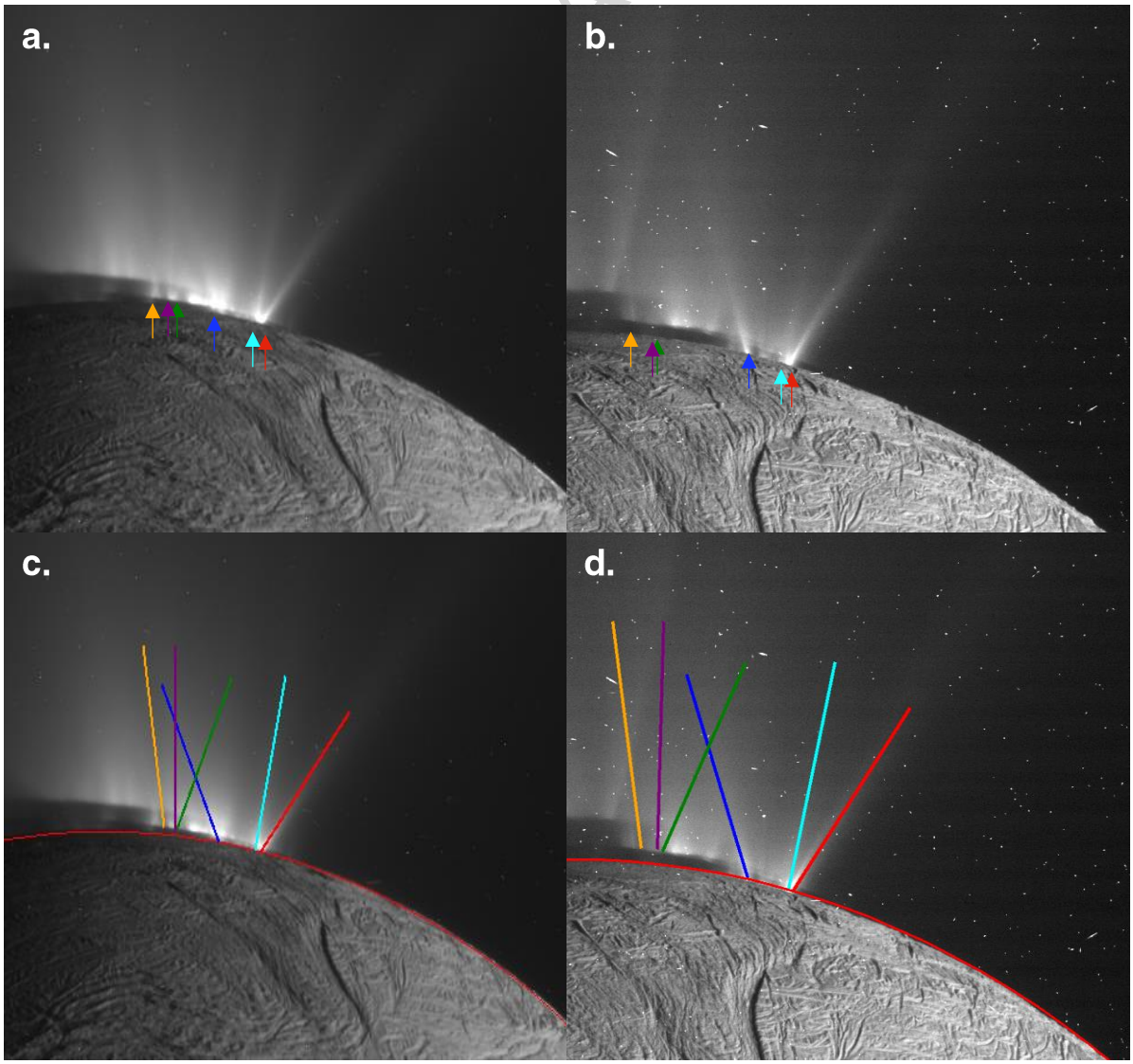

FIGURE 8. EXAMPLE OF JETS TURNING ON AND OFF. THE FIGURE WAS CONSTRUCTED FROM TWO IMAGES, LEFT AND RIGHT, TAKEN 20 DAYS APART AT NEARLY THE SAME VIEWING GEOMETRY. THE IMAGES ARE REPEATED IN THE BOTTOM ROW WITH DIFFERENT GRAPHICS. PANELS (A) AND (C) ARE IMAGE N1669801210_1, WHICH WAS TAKEN ON NOVEMBER 30, 2010 AT A SUB-SPACECRAFT LONGITUDE OF 63° AND MA = 61°. PANELS (B) AND (D) ARE IMAGE N1671582609_1, WHICH WAS TAKEN ON DECEMBER 20, 2010 AT A SUB-SPACECRAFT LONGITUDE OF 49º AND MA = 71º. IN THE TOP ROW (PANELS A AND B) THE ARROWS INDICATE THE EXPECTED LOCATIONS OF INDIVIDUAL JETS FROM TABLE 2 OF PORCO ET AL. (2014). IN THE BOTTOM ROW (PANELS C AND D) THE SAME JETS ARE SHOWN AS 50-KM COLORED LINES PROJECTED ONTO THE IMAGE PLANE USING THE COORDINATES AND TILTS FROM TABLE 2 OF PORCO ET AL. (2014). THE SUN IS BELOW THE HORIZON, WHICH IS INDICATED BY THE RED CURVE. THE FOREGROUND IS ILLUMINATED BY LIGHT FROM SATURN. TIGER STRIPES IN THE FOREGROUND EMIT CURTAINS WHOSE BASES ARE IN SHADOW, GIVING THE APPEARANCE OF MULTIPLE DARK HORIZONS. THIS ALLOWS US TO DIFFERENTIATE BETWEEN SUPERPOSED SOURCES EMANATING FROM DIFFERENT TIGER STRIPES. THE JET ID NUMBERS IN PORCO ET AL. (2014) AND THE COLORS IN THE FIGURE ARE: 1 (RED), 2 (CYAN), 5 (BLUE), 34 (PURPLE), 35 (GREEN), AND 36 (YELLOW). THE GREEN AND PURPLE JETS APPEAR TO HAVE TURNED OFF IN THE 20 DAYS BETWEEN THE LEFT AND THE RIGHT IMAGES, AND THE CYAN JET APPEARS TO HAVE WEAKENED. AN UNIDENTIFIED JET WHOSE BASE IS NEAR THE LEFT EDGE CAN BE SEEM SLANTING UPWARD TO THE RIGHT IN THE DECEMBER 20 IMAGE. THIS JET WAS MISTAKENLY IDENTIFIED AS JET 12 OF CAIRO IN FIGURE 4 OF PORCO ET AL. (2014). HOWEVER, WE SEE HERE FROM THE SHADOW GEOMETRY THAT THE JET ACTUALLY ORIGINATES ON DAMASCUS NEAR -80° LATITUDE AND 313° WEST LONGITUDE.

FIGURES 8 AND 9 SHOW IMAGES TAKEN 20 DAYS APART AND 42 DAYS APART, RESPECTIVELY. THEY BOTH SHOW ABOUT 10 DISTINCT JETS OR CENTERS OF ACTIVITY, AND ALMOST HALF OF THEM APPEAR TO HAVE

CHANGED. FIGURE 8 DETAILS THE DISAPPEARANCE OF TWO DISTINCTLY COLLIMATED JETS, 34 AND 35 FROM PORCO ET AL. (2014) TABLE 2. SEVERAL JETS ARE CONSISTENT ACROSS THE TWO IMAGES. FIGURE 9 SHOWS A COMPLEMENTARY EXAMPLE, IN WHICH JET 10 FROM THE PORCO ET AL. (2014) CATALOG TURNS ON OVER A SIMILAR TIMESCALE. AGAIN, MULTIPLE JETS appear consistent across both images of Figure 9, but this single jet appears to vary independently. In principle, the apparent presence or absence of jets can be influenced by the particular viewing geometry of an image. However, the viewing geometries of the images considered here are quite similar (<25° rotation) and multiple jets remain visible at consistent orientations between the images in each pair. These similarities, combined with the fact that our routine accounts for differences in the apparent tilt and foreshortening of individual jets due to the image geometries, suggest that viewing geometry effects are likely not the cause of the individual jet variability we observe. INTERESTINGLY, THE MEAN ANOMALY OF ENCELADUS IS NEARLY THE SAME ACROSS ALL OF THESE OBSERVATIONS, SUGGESTING THAT THE MECHANISM THAT CONTROLS THIS VARIABILITY IS INDEPENDENT OF THAT WHICH CONTROLS THE OVERALL PLUME BRIGHTNESS ON DIURNAL TIMESCALES.

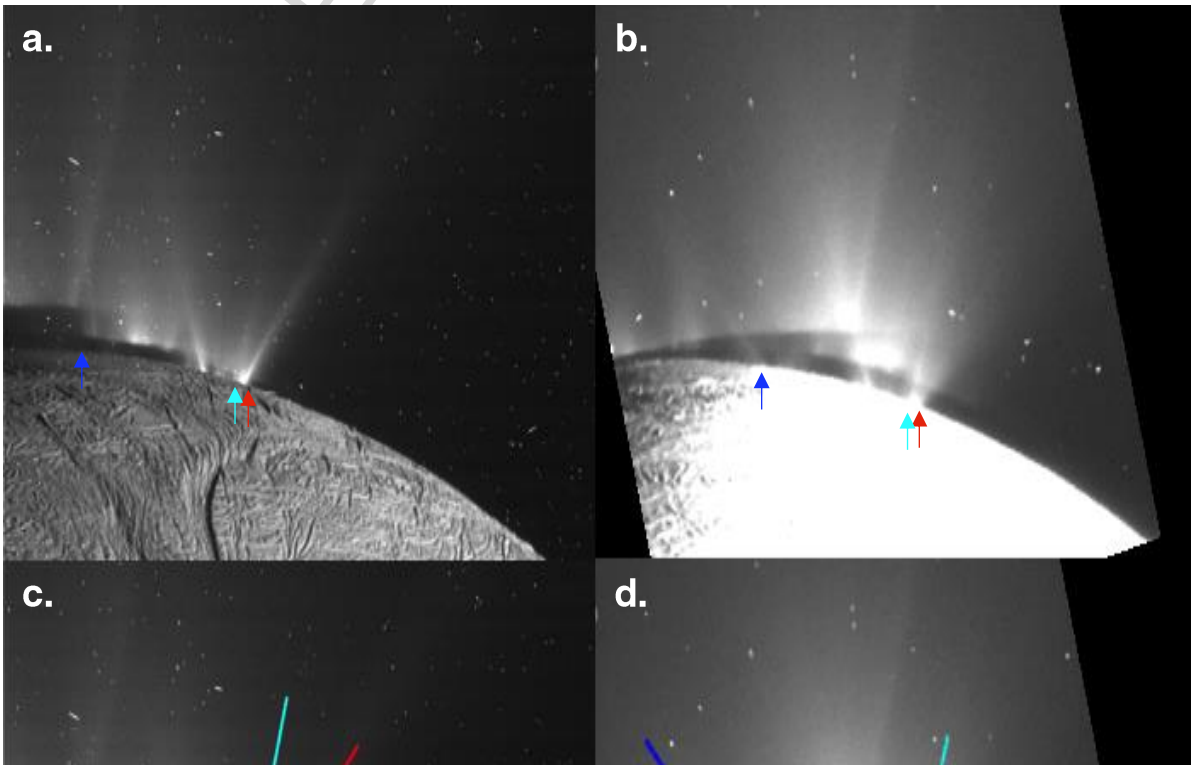

FIGURE 9. AN EXAMPLE OF A JET TURNING ON. THE LAYOUT IS AS IN FIGURE 8, EXCEPT THE FIRST MEMBER OF THE PAIR, IN PANELS (A) AND (C), IS THE LAST MEMBER OF THE PAIR IN FIGURE 8. THE SECOND MEMBER OF THE PAIR, IN PANELS (B) AND (D) IS IMAGE N1675142316_1, WHICH WAS TAKEN ON JANUARY 31 2011 AT A SUB-SPACECRAFT LONGITUDE OF 72º AND MA = 79°. THUS, THE IMAGES WERE TAKEN 42 DAYS APART. THE JET ID NUMBERS IN PORCO ET AL. (2014) AND THE COLORS IN THE FIGURE ARE: 1 (RED), 2 (CYAN), AND 10 (BLUE). IN THE TIMESPAN BETWEEN THE TWO IMAGES, THE BLUE JET HAS TURNED ON WITH A HIGHLY COLLIMATED APPEARANCE. IN CONTRAST, THE RED JET HAS SPREAD OUT AND BECOME LESS COLLIMATED.

THE ~MONTH-LONG TIMESCALE IS COMPATIBLE WITH WHAT IP10 AND NI16 ESTIMATED FOR CRACKS SEALING THEMSELVES OFF, ALTHOUGH IT DOES NOT PROVE THAT THEIR MECHANISM - ICE BUILDUP ON THE WALLS - IS CAUSING THE VARIABILITY. A SECONDARY OBSERVATION FROM FIGURE 9 MAY PROVIDE A CLUE—WHILE THE NEWLY APPEARED JET (BLUE) IS HIGHLY COLLIMATED, AN OLDER WEAKENED JET (RED) APPEARS TO HAVE SPREAD OUT AND LOST ITS COLLIMATION. A TENDENCY OF NEW JETS TO BE HIGHLY COLLIMATED MIGHT TELL US SOMETHING ABOUT HOW THE JETS RE-ESTABLISH THEMSELVES, THEREBY COMPLETING THEIR LIFE CYCLES. YEOH ET AL. (2017) FIND THAT THE HIGHLY COLLIMATED JETS ARISE FROM DEEP UNDERGROUND SOURCES WITH LARGE VARIATIONS IN CHANNEL WIDTH. THE LARGE VARIATIONS (AS OPPOSED TO FAIRLY STRAIGHT CHANNELS) ALLOW THE GAS TO EXPAND TO HIGH MACH NUMBERS AT THE VENT. EVOLUTION OF THE JETS IS UNDOUBTEDLY TIED TO

EVOLUTION OF THE CHANNELS. FIGURES 8 AND 9 ARE TELLING US ABOUT EVOLUTION OF BOTH KINDS. FOR FURTHER RESULTS AND DISCUSSION, SEE GOLDSTEIN ET AL. (2018).

Many of the 2,405 images were taken too far from Enceladus to reliably distinguish individual jets, and only a few exist at high spatial resolution and similar viewing geometries. However, within the observations we found suitable to compare (which number less than 15 across varying degrees of suitability), we see evidence for discrete, aperiodic variability in all of them.

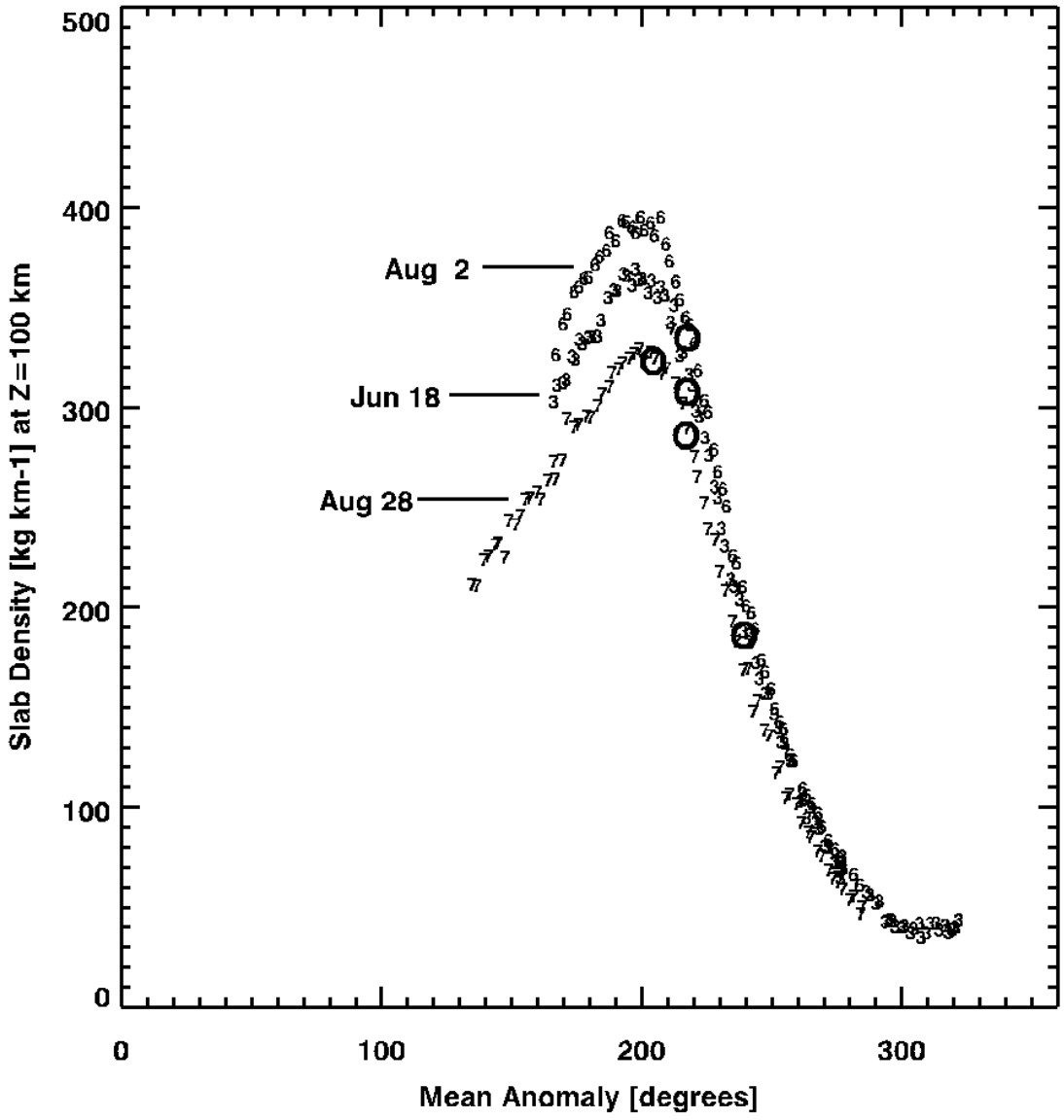

FIGURE 10. SLAB DENSITY AT 100 KM ALTITUDE VS. MA ON JUNE 18, 2017, AUGUST 2, 2017, AND AUGUST 28, 2017. EACH DAY PRODUCED A STREAM OF OBSERVATIONS LASTING MORE THAN HALF A DAY AND COVERING AT LEAST 117 DEGREES OF LONGITUDE (TABLE 1). THE IMAGE PROCESSING TECHNIQUES AND THE ASSUMED PARTICLE SIZE DISTRIBUTION WERE THE SAME FOR THE ENTIRE DATA SET. THE SMOOTHNESS OF THE CURVES IS EVIDENCE THAT THE MEASUREMENT PRECISION IS MUCH SMALLER THAN THE DIFFERENCE BETWEEN THE THREE JETS. THE FIVE HEAVY CIRCLES IDENTIFY THE IMAGES SHOWN IN FIGURE 11. THE THREE IN A VERTICAL LINE

at MA = 233° are from the bottom row of Figure 11. The circles at MA = 216° and 259° have the same -80° sub-spacecraft longitude as the middle circle at MA = 233° and are from the top row of Figure 11. Table 3 gives further information about these five images.

The relative strength of the discrete jets as opposed to the curtains distributed along the tiger stripes (Spitale et al., 2015) is a separate issue. Yeoh et al. (2017) find that the model that has only tiger stripes provides a good fit to the UVIS data, and they conclude that the jets are a lesser source of plume vapor. Figures 10 and 11 address this issue for the ice particles in the plume. Figure 10 shows plume brightness vs. MA for three days in 2017 - June 18, August 2, and August 28. Each day covered the range from MA = 150° to MA = 300°, which means they covered the plume maximum around MA = 200°. The figure shows that the inferred slab density was 10% greater in the middle of the sequence - on August 2 - than it was at the beginning or the end. Whether this was due to a jet that turned on and off is not clear from the figure. On the other hand, the center column of Figure 11 shows a highly collimated jet that was present on August 2 but not on June 18 or August 28. By comparing slab density integrated to $\pm \infty$ in the horizontal direction to the portion of the integral that only includes the jet, we estimate that the jet was contributing 3% to the slab density at 100 km. The left and right columns of Figure 11 show that the jet was not present on June 16 and August 28 in images taken at the same MA or in images taken at the same sub-spacecraft longitude. Regardless of the role of the jet, the important result from Figure 10 is that the slab density, which samples all the particles in the plume at a given altitude, rose and fell by 10% during this 71-day interval.

	2017 JUN 16 (day 3)	2017 AUG 2 (day 6)	2017 AUG 28 (day 7)
Image number	N1876468904_1	N1880373431_1	N1882621525_1
MA	259	233.175	216
s/c lon (same across)	-79.957	-79.929	-80.124

Image number	N1876461704_1	(same above)	N1882625653_1
MA (same across)	233.212	233.175	232.690
s/c lon	-60	-79.929	-92

TABLE 3. PROPERTIES OF THE IMAGES IN FIGURE 11. THE TABLE AND THE FIGURE ARE ARRANGED AS 3X2 MOSAICS, AND THE RELATIVE LOCATIONS OF THE IMAGES ARE THE SAME.

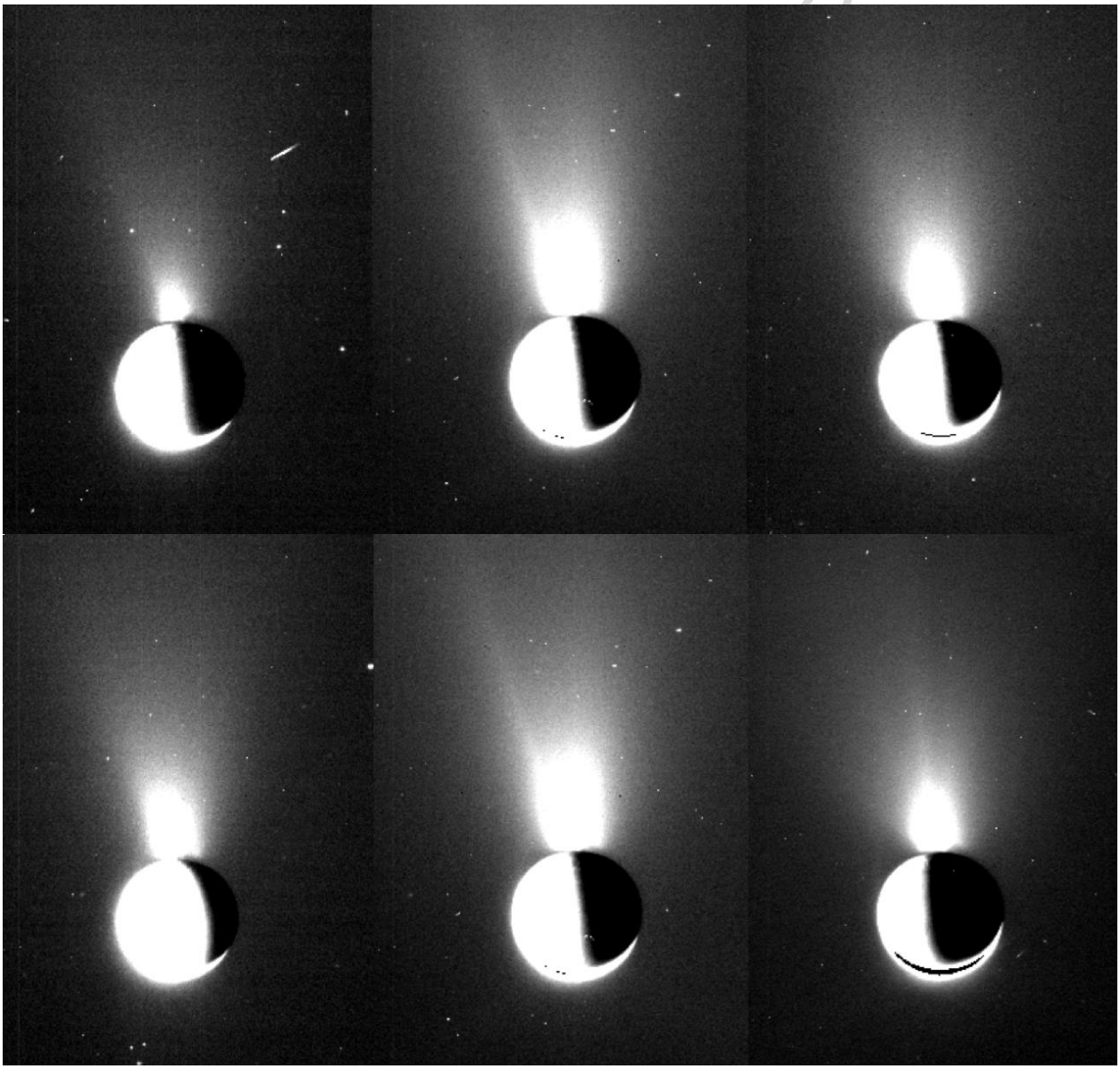

Figure 11. Isolated jet that appeared on August 2, 2017 (center) but was absent on June 18, 2017 (left) and August 28, 2017 (right). The center is Image N1880373431_1, and it is repeated top and bottom. The top row of images have the same sub-spacecraft longitude. The bottom row of images have the same MA. The jet originates to the left of the terminator, on the sunlit side, and is tilted to the left at higher altitudes (center column). By itself, this jet contributes about 3% to the slab density at 100 km. The contrast stretch is the same for all images and was chosen to bring out details of the jet, which caused saturation at the base of the jet. The original images were not saturated. The jet remained visible for 1/3 of a day and 117° of spacecraft longitude, so it was not a curtain seen edge-on like those seen by Spitale et al. (2015). Image numbers, MAs, and sub-spacecraft longitudes of the images are given in Table 3.

5. Particle velocity

The falloff of plume brightness with altitude, first noted by Hedman et al. (2013), is an inverse measure of particle velocity near the vent. Porco et al. (2006) reported a mean velocity of 60 m s^{-1}, which is only 25% of the thermal velocity of the vapor and/or the escape velocity of Enceladus. To explain the low velocities, Schmidt et al. (2008) offered a model in which the particles are colliding with the walls every 0.1 m and don't have time to accelerate to the speed of the gas before they escape. Hedman et al. (2013) report that the brightness falloff with altitude is greatest at apocenter, meaning that the velocity at the vent is lowest there. In contrast, Nimmo et al. (2014) say there is no systematic variation in scale height either with plume brightness or with Enceladus' orbital position. IE17 report that the brightness roughly follows a $z^{-\alpha}$ power law in the altitude range 50-200 km, where z is altitude above the south pole. They find on average that $\alpha \approx 1/3$, but near apocenter α is larger, up to 1/2, in qualitative agreement with Hedman et al. (2013) but not with Nimmo et al.

(2014). IE17 use three possible velocity distributions to fit the data - exponential, Gaussian, and Lorentzian. They find median velocities at the vent of 143-150 m s^{-1} in all cases.

Figure 12 shows dlogS/dlogz, where S is slab density and z is altitude. The secondary maximum, which occurs in the range MA = 25-60°, has the least negative values of dlogS/dlogz (smallest value of alpha), indicating that the particles are launched with a higher velocity there than in other parts of the orbit. Conversely, the points near MA = 140° have the most negative values of dlogS/dlogz (largest value of alpha), indicating that the particles are launched with a lower velocity there than in the rest of the orbit. This figure reinforces the conclusion noted by Hedman and IE17, that the launch velocity is low when the mass flux is high, but it shifts the MA of minimum wind speed slightly earlier, from MA = 180° to MA = 140°. The difference between the black (2017) points and the light blue, orange and red (2009-2015) points from MA = 150-230°.is real, and shows up no matter how we process the data. We have no definite explanation for this feature, but we suspect it represents a real increase in launch velocity from the years 2009-2015 to the year 2017. With only these data, it is difficult to say whether this this increase in launch velocity is related to the 3.9- and 11.1-years cycles or not.

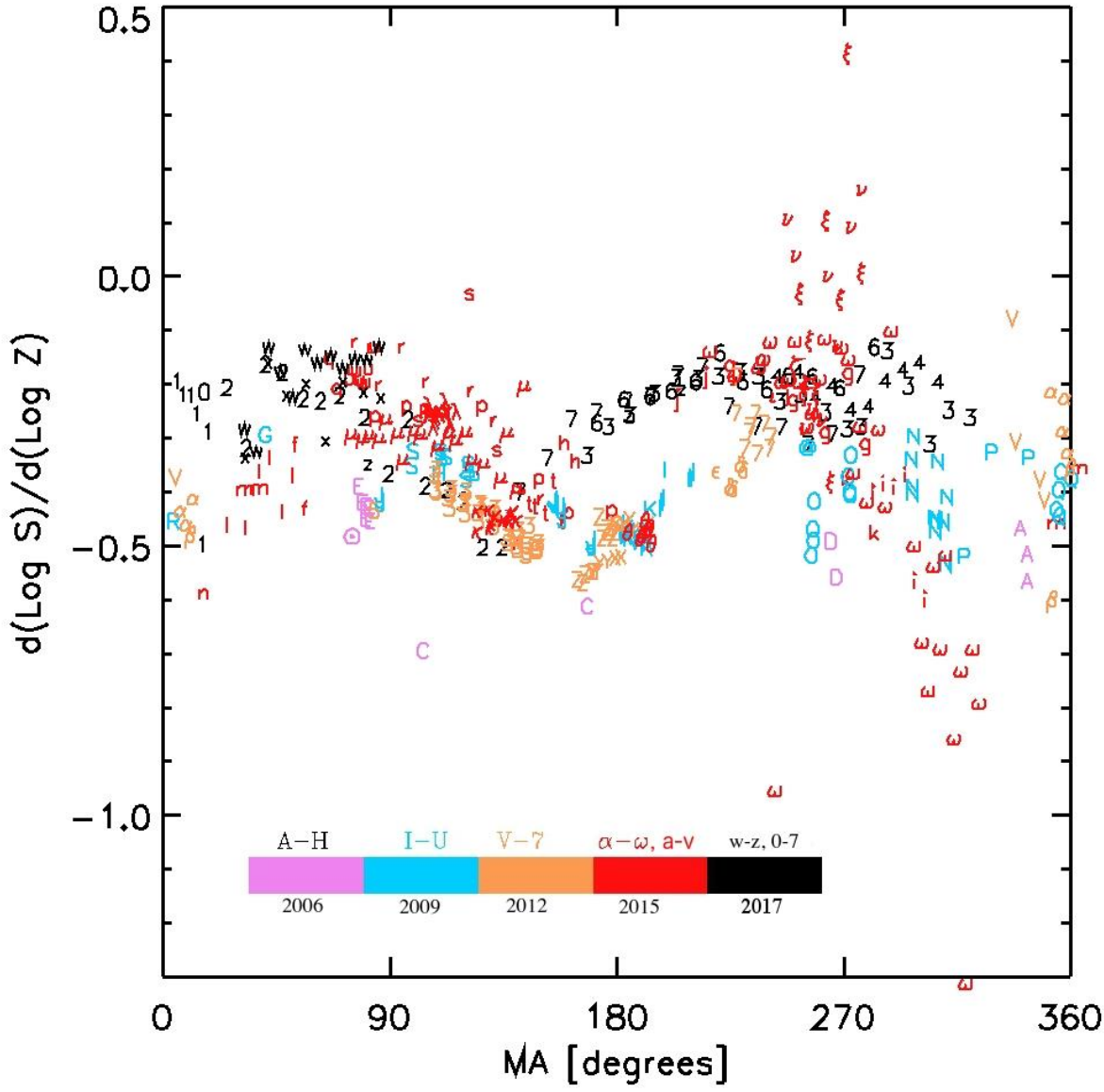

FIGURE 12. EXPONENT -α IN THE RELATION $S \propto Z^{-\alpha}$ WHERE S IS SLAB DENSITY AND Z IS ALTITUDE. THE ALPHANUMERIC SYMBOLS AND THE COLORS ARE THE SAME AS IN FIGURE 1. EACH CHARACTER ON THE GRAPH REPRESENTS A SINGLE IMAGE, WITH MEASUREMENTS AT Z = 50, 70, 100, 140, AND 200 KM. THESE FIVE MEASUREMENTS WERE FITTED TO A STRAIGHT LINE IN LOGS VS. LOG Z SPACE. THE SLOPE OF THE LINE DETERMINES THE HEIGHT OF THAT DAY'S POINT ON THE GRAPH. HIGHER ON THE GRAPH (LESS NEGATIVE VALUES OF -α) MEANS A HIGHER LAUNCH SPEED. FOR EACH DAY THE STATISTICAL UNCERTAINTY OF THE SLOPE WAS CALCULATED BY ASSUMING EACH

measurement of log S is independent of the other four, and the underlying relation is a straight line. The standard deviation for each point of Figure 12 is shown in Figure S1 in the Supplementary Material and follows section 14.2 of Press et al. (1986). Typically, the standard deviation of the slope is about 0.05 except for the red ω and ν points, which have low SNR as discussed following Figure 1 and therefore have a large uncertainty. Figure 12 shows all observations from 2005 to 2017.

6. Discussion

We have shown that the 5% peak-to-peak excursion in orbital eccentricity is associated with a 2-fold excursion in plume brightness. The excursion in eccentricity is associated with the resonance with Dione and manifests itself as two superposed oscillations with periods of 3.9 and 11.1 years. The question arises, why should such a relatively small forcing lead to a relatively large response? Has the system arranged itself into a self-organized critical state? Also, why should the 3.9 and 11.1 year oscillations manifest themselves as a single multiplicative factor controlling the amplitude of the diurnal cycle?

We have shown that the diurnal swings (coinciding with the orbit period) of the vapor plume measured by UVIS are more than a factor of 2, and they match up with the diurnal swings of the particle plume measured by ISS. The decadal swings also match up. But the two components of the plume have different average speeds, by a factor of 5 or more. This seems inconsistent with the argument of Yeoh et al. (2015) that the particles should remain coupled to the vapor at the vents. Are particle collisions with the walls every 10 cm the answer, as Schmidt et al. (2008) have argued? Are tortuous cracks and frequent collisions compatible with the high speed (Mach number > 5) of the gas, as inferred by Yeoh et al. (2017)? Or are the particles forming where the gas is rapidly expanding, leaving the particles behind?

We have shown that individual plumes are varying from month to month, which roughly matches the time scale of the vents plugging themselves with ice, as proposed by IP10. But how do the vents turn themselves on again? Or are new jets constantly arising? Is it possible that the ice flows outward when the vents are pressed shut, thereby maintaining a constant width when they are open?

We have shown that the particle velocity is least at points in the orbit where the particle mass flux is greatest. What feature of the underground plumbing is causing this to happen, and is it consistent with particle collisions with the walls and lateral flow of the ice? There is evidence that particle launch velocity is varying from year, at least in the range around MA = 180°. Why would this happen, and could it be related to the 3.9- and 11.1-year cycles?

One could invent more questions, but one cannot gather more Cassini data. Many of these questions could be answered by theoretical modeling. We are attracted to the idea of Kite and Rubin (2016), that the ~ 5.8 GW of radiated power is from turbulent dissipation associated with the daily flushing and refilling of the cracks. They show that the heat generated and the mechanical disruption could stave off freezing. However, Kite and Rubin did not pursue the full implications of their model - the possibility that the liquid-vapor interface could rise to the surface at some point during the diurnal cycle. This would significantly affect the phase curve of plume activity, and it opens up the possibility of two-way exchange between the surface and the ocean. Such exchange could increase the habitability of Enceladus as Parkinson et al. (2008) have suggested. Liquid water flowing up and down could account for the secondary maximum, since water is squeezed toward the surface when the cracks are closing, leading to a high evaporation rate and a peak in the mass flux. Liquid water would develop a thin icy crust in a few minutes when exposed to

vacuum. Using Cassini VIMS data, Goguen et al. (2013) infer a temperature of 197 ± 20 K across a fissure 9 m wide, but they point out that such temperatures cannot persist for more than a few days. Liquid water might persist under an icy crust, but the details have not been worked out.

The main peak in the mass flux occurs when the cracks are open and the evaporating area is largest. To the best of our knowledge, Ingersoll and Nakajima (2016) are the only group besides Kite and Rubin who have tried to model the flow of the liquid. These models presuppose there are liquid-filled cracks extending through the ice to the ocean. Other configurations are possible, and more models are needed. We are confident that the models, constrained by Cassini data, will tell us about the ocean and its connection to the moon's surface.

Acknowledgements

This research was supported by the National Aeronautics and Space Administration through the Cassini Project Office and through the Cassini Data Analysis Program grant number NNX15AH08G.

References

Abramov, O., & Spencer, J. R. (2009). Endogenic heat from Enceladus' south polar fractures: New observations, and models of conductive surface heating. *Icarus*, *199*(1), 189–196. https://doi.org/10.1016/j.icarus.2008.07.016

Dong, Y., Hill, T. W., & Ye, S.-Y. (2015). Characteristics of ice grains in the Enceladus plume from Cassini observations. *Journal of Geophysical Research-Space Physics*, *120*(2), 915–937. https://doi.org/10.1002/2014JA020288

Gao, P., Kopparla, P., Zhang, X., & Ingersoll, A. P. (2016). Aggregate particles in the plumes of Enceladus. *Icarus*, *264*, 227–238. https://doi.org/10.1016/j.icarus.2015.09.030

Goldstein, D. B., Hedman, M., Manga, M., Perry, M., Spitale, J., (2018). Enceladus plume dynamics: From surface to space. In: Schenk, P., Clark, R. N., Howett, C. J. A., Verbiscer, A. J., Waite, J. H. (Eds.), Enceladus and the Icy Moons of Saturn. University of Arizona Press, Tucson, pp. 175-194. ISBN 9780816537075.

Hansen, C. J., Shemansky, D. E., Esposito, L. W., Stewart, A. I. F., Lewis, B. R., Colwell, J. E., et al. (2011). The composition and structure of the Enceladus plume. *Geophysical Research Letters*, *38*, L11202. https://doi.org/10.1029/2011GL047415

Hansen, C. J., Esposito, L. W., Aye, K.-M., Colwell, J. E., Hendrix, A. R., Portyankina, G., & Shemansky, D. (2017). Investigation of diurnal variability of water vapor in Enceladus' plume by the Cassini ultraviolet imaging spectrograph. *Geophysical Research Letters*, *44*(2), 672–677. https://doi.org/10.1002/2016GL071853

Hedman, M. M., Gosmeyer, C. M., Nicholson, P. D., Sotin, C., Brown, R. H., Clark, R. N., et al. (2013). An observed correlation between plume activity and tidal stresses on Enceladus. *Nature*, *500*(7461), 182–184. https://doi.org/10.1038/nature12371

Hedman, M. M., Dhingra, D., Nicholson, P. D., Hansen, C. J., Portyankina, G., Ye, S., & Dong, Y. (2018). Spatial variations in the dust-to-gas ratio of Enceladus' plume. *Icarus*, *305*, 123–138. https://doi.org/10.1016/j.icarus.2018.01.006

Helfenstein, P., & Porco, C. C. (2015). Enceladus' Geysers: Relation to Geological Features. *Astronomical Journal*, *150*(3), 96. https://doi.org/10.1088/0004-6256/150/3/96

Hurford, T. A., Helfenstein, P., Hoppa, G. V., Greenberg, R., & Bills, B. G. (2007). Eruptions arising from tidally controlled periodic openings of rifts on Enceladus. *Nature*, *447*(7142), 292–294. https://doi.org/10.1038/nature05821

Ingersoll, A. P., & Ewald, S. P. (2011). Total particulate mass in Enceladus plumes and mass of Saturn's E ring inferred from Cassini ISS images. *Icarus*, *216*(2), 492–506. https://doi.org/10.1016/j.icarus.2011.09.018

Ingersoll, A. P., & Ewald, S. P. (2017). Decadal timescale variability of the Enceladus plumes inferred from Cassini images. *Icarus*, *282*, 260–275. https://doi.org/10.1016/j.icarus.2016.09.018

Ingersoll, A. P., & Nakajima, M. (2016). Controlled boiling on Enceladus. 2. Model of the liquid-filled cracks. *Icarus*, *272*, 319–326. https://doi.org/10.1016/j.icarus.2015.12.040

Ingersoll, A. P., & Pankine, A. A. (2010). Subsurface heat transfer on Enceladus: Conditions under which melting occurs. *Icarus*, *206*(2), 594–607. https://doi.org/10.1016/j.icarus.2009.09.015

Kite, E. S., & Rubin, A. M. (2016). Sustained eruptions on Enceladus explained by turbulent dissipation in tiger stripes. *Proceedings of the National Academy of Sciences of the United States of America*, *113*(15), 3972–3975. https://doi.org/10.1073/pnas.1520507113

Nakajima, M., & Ingersoll, A. P. (2016). Controlled boiling on Enceladus. 1. Model of the vapor-driven jets. *Icarus*, *272*, 309–318. https://doi.org/10.1016/j.icarus.2016.02.027

Nimmo, F., Porco, C., & Mitchell, C. (2014). Tidally Modulated Eruptions on Enceladus: Cassini Iss Observations and Models. *Astronomical Journal*, *148*(3), 46. https://doi.org/10.1088/0004-6256/148/3/46

Parkinson, C. D., Liang, M.-C., Yung, Y. L., & Kirschivnk, J. L. (2008). Habitability of Enceladus: Planetary conditions for life. *Origins of Life and Evolution of Biospheres*, *38*(4), 355–369. https://doi.org/10.1007/s11084-008-9135-4

Porco, C., DiNino, D., & Nimmo, F. (2014). How the Geysers, Tidal Stresses, and Thermal Emission Across the South Polar Terrain of Enceladus Are Related. *Astronomical Journal*, *148*(3), 45. https://doi.org/10.1088/0004-6256/148/3/45

Porco, C., Mitchell, C., Nimmo, F., & Tiscareno, M. (2018). Enceladus' plume temporal variability from analysis of Cassini ISS images. *Lunar and Planetary Sci. Conf. 2018*, 2083.

Porco, C. C., Helfenstein, P., Thomas, P. C., Ingersoll, A. P., Wisdom, J., West, R., et al. (2006). Cassini observes the active South Pole of Enceladus. *Science*, *311*(5766), 1393–1401. https://doi.org/10.1126/science.1123013

Press, W. H., Flannery, B. P., Teukolsky, S. A., Vetterling, W. T., (1986). Numerical Recipes. Cambridge University Press, Cambridge, UK. ISBN 0 521 30811 g.

Schmidt, J., Brilliantov, N., Spahn, F., & Kempf, S. (2008). Slow dust in Enceladus' plume from condensation and wall collisions in tiger stripe fractures. *Nature*, *451*(7179), 685–688. https://doi.org/10.1038/nature06491

Spencer, J. R., Pearl, J. C., Segura, M., Flasar, F. M., Mamoutkine, A., Romani, P., et al. (2006). Cassini encounters Enceladus: Background and the discovery of a south polar hot spot. *Science*, *311*(5766), 1401–1405. https://doi.org/10.1126/science.1121661

Spencer, J. R., Nimmo, F., Ingersoll, A. P., Hurford, T. A., Kite, E. S., Rhoden, A. R., Schmidt, J., Howett, C. J. A., (2018). Plume origins and plumbing: From ocean to surface. In: Schenk, P., Clark, R. N., Howett, C. J. A., Verbiscer,

A. J., Waite, J. H. (Eds.), Enceladus and the Icy Moons of Saturn. University of Arizona Press, Tucson, pp. 163-174. ISBN 9780816537075.

Spitale, J. N., Hurford, T. A., Rhoden, A. R., Berkson, E. E., & Platts, S. S. (2015). Curtain eruptions from Enceladus' south-polar terrain. *Nature*, *521*(7550), 57-U368. https://doi.org/10.1038/nature14368

Teolis, B. D., Perry, M. E., Magee, B. A., Westlake, J., & Waite, J. H. (2010). Detection and measurement of ice grains and gas distribution in the Enceladus plume by Cassini's Ion Neutral Mass Spectrometer. *Journal of Geophysical Research-Space Physics*, *115*, A09222. https://doi.org/10.1029/2009JA015192

Teolis, B. D., Perry, M. E., Hansen, C. J., Waite, J. H., Porco, C. C., Spencer, J. R., & Howett, C. J. A. (2017). Enceladus Plume Structure and Time Variability: Comparison of Cassini Observations. *Astrobiology*, *17*(9), 926–940. https://doi.org/10.1089/ast.2017.1647

Vienne, A., & Duriez, L. (1991). A General-Theory of Motion for the 8 Major Satellites of Saturn .2. Short-Period Perturbations. *Astronomy & Astrophysics*, *246*(2), 619–633.

Yeoh, S. K., Chapman, T. A., Goldstein, D. B., Varghese, P. L., & Trafton, L. M. (2015). On understanding the physics of the Enceladus south polar plume via numerical simulation. *Icarus*, *253*, 205–222. https://doi.org/10.1016/j.icarus.2015.02.020

Yeoh, S. K., Li, Z., Goldstein, D. B., Varghese, P. L., Levin, D. A., & Trafton, L. M. (2017). Constraining the Enceladus plume using numerical simulation and Cassini data. *Icarus*, *281*, 357–378. https://doi.org/10.1016/j.icarus.2016.08.028

Highlights

- The particle plume varies by a factor of ten as part of the diurnal cycle
- The particle plume varies as a mixture of 3.9- and 11.1-year cycles in eccentricity
- The particle and vapor plumes may be varying together with constant mass ratio
- Individual particle jets have lifetimes as short as several months
- The particle launch velocity has varied on a timescale of several years